# Controls on Physical and Chemical Denudation in a Mixed Carbonate-Siliciclastic Orogen

**E. D. Erlanger[1], J. K. C. Rugenstein[2], A. Bufe[1], V. Picotti[3], and S. D. Willett[3]**

[1]GFZ, Telegrafenberg, Potsdam, Germany

[2]Department of Geosciences, Colorado State University, Fort Collins, CO 80521, USA

[3]Department of Earth Sciences, ETH Zürich, Zürich, Switzerland

Erica Erlanger (ederlanger@gmail.com)

**Key Points:**

- Quantify chemical weathering and physical erosion fluxes for a mixed-lithology mountain range
- Physical erosion dominates the denudation signal and carbonate weathering dominates the weathering signal
- Precipitation of secondary carbonate is responsible for the loss of up to 90% of dissolved [$Ca^{2+}$] in carbonate-rich rivers.
- Up to 90% of chemically weathered $Ca^{2+}$ is precipitated as solid secondary carbonate that becomes part of physical denudation flux

## Abstract

Mixed siliciclastic and carbonate active orogens are common on Earth's surface, yet most studies have focused on physical erosion and chemical weathering in silicate-rich landscapes. Relative to purely siliciclastic landscapes, the response of erosion and weathering to uplift may differ in mixed-lithology regions. However, our knowledge of weathering and erosion in mixed carbonate-silicate lithologies is limited and thus our understanding of the mechanistic coupling between uplift, chemical weathering, and the carbon cycle. Here, we partition the denudation fluxes into erosion and weathering fluxes of carbonates and silicates in the Northern Apennine Mountains of Italy—a mixed siliciclastic-carbonate active orogen—using dissolved solutes, the fraction of carbonate sand in sediments, and existing $^{10}$Be denudation rates. Erosion fluxes are generally an order of magnitude higher than weathering fluxes and dominate total denudation. The contribution of carbonate and silicate minerals to erosion varies between lithologic units, but weathering fluxes are systematically dominated by carbonates. Silicate weathering may be limited by reaction rates, whereas carbonate weathering may be limited by acidity of the rivers that drain the orogen. Precipitation of secondary calcite from super-saturated streams leads to the loss of up to 90% of dissolved $Ca^{2+}$ from carbonate-rich catchments. Thus, in the weathering zone, $[Ca^{2+}]$ is exceptionally high, likely driven by high soil $pCO_2$; however, re-equilibration with atmospheric $pCO_2$ in rivers converts solutes back into solid grains that become part of the physical denudation flux. Limits on weathering in this landscape therefore differ between the subsurface weathering zone and what is exported by rivers.



## Plain Language Summary

Erosion moves sediment across the surface and controls how natural resources (e.g. sand and gravel) are generated. Conversely, the dissolution of rock in water (weathering) is the source for nutrients and carbon transported in rivers. Understanding how total surface lowering (denudation) is divided into weathering and erosion is important for establishing the link between mountain-building processes and the generation of sediments and dissolved material.

Existing studies on denudation in mountainous ranges have primarily focused on landscapes comprised of silicate rocks. However, many mountain ranges are characterized by mixed silicate-

carbonate rocks, and the processes that influence denudation of these landscapes may differ relative to silicate-rich landscapes.

In this study, we separate measurements of denudation into erosion and weathering for the Northern Apennine Mountains of Italy, a mixed-lithology mountain range. Similar to silicate-rich landscapes, erosion is the dominant process here. Carbonate weathering dominates the total weathering signal, and rock type is an important control on the amount of eroded carbonate delivered to river channels. Most rivers are oversaturated in carbonate, therefore limiting the amount that can be dissolved in rivers. This has resulted in the transformation of dissolved material back into carbonate rock that is once again available to be eroded.

## 1 Introduction

Tectonically active orogens are responsible for the majority of sediments and solutes delivered annually to the world's oceans (Milliman and Farnsworth, 2011; Larsen et al., 2014). Fresh rock uplifted in mountain ranges is broken down by chemical weathering and physical erosion, thereby creating soils, sediments, and solutes. Driven by topographic gradients, runoff then transports these sediments and solutes to the surrounding floodplains and to the ocean. This process is so fundamental to the cycling of rocks, nutrients, and carbon on Earth that changes in the activity or spatial distribution of active orogens is frequently invoked to explain a variety of phenomenon observed throughout Earth's history. For example, periods of icehouse and greenhouse climates have been attributed to tectonic activity, because the uplift and erosion of rock generates fresh mineral surfaces that become available for silicate weathering, thereby modulating atmospheric $CO_2$ concentrations (Goddéris et al., 2017; Caves Rugenstein et al., 2019).

The interplay between physical erosion and chemical weathering and its impact on the geological carbon cycle is fundamentally controlled by the type of lithology that is exposed and eroded. Previous studies on denudation fluxes in orogenic landscapes have focused on settings with silicate-rich bedrock (Brandon and Vance, 1992; Granger et al., 1996; Kirchner et al., 2001; Jacobson and Blum, 2003; Jacobson et al., 2003; Matmon et al., 2003; Moore et al., 2013; Carretier et al., 2015; Emberson et al., 2017). In these landscapes, physical erosion fluxes

typically dominate the denudation signal by an order of magnitude relative to chemical weathering fluxes (Riebe et al., 2001; Jacobson and Blum, 2003; West et al., 2005). Silicate weathering fluxes are thought to increase with increasing denudation rates up to a limit, at which point the sluggish kinetics of silicate dissolution lag behind the exposure of fresh mineral surfaces (West et al., 2005; Gabet and Mudd, 2009). However, many active orogens today are underlain not by pure silicate bedrock, but by either carbonate rock or interbedded siliciclastic and carbonate sediments. The partitioning of denudation into physical erosion and chemical weathering in these lithologies may be fundamentally different than the partitioning in silicate-rich terranes. For example, the dissolution kinetics of carbonates are more than three orders of magnitude faster than for silicates (Stallard and Edmond, 1987), and weathering fluxes are globally dominated by carbonate weathering (Gaillardet et al., 1999). Even in places where carbonate constitutes a minor component of the bedrock, carbonate weathering is frequently the dominant source of cations (Sarin et al., 1989; Jacobson and Blum, 2003; Calmels et al., 2007; Torres et al., 2016; Hilton and West, 2020). Importantly, carbonate and silicate weathering produce different nutrients and soils (Ott, 2020) and differ in their impact on the carbon cycle. Whereas silicate weathering is a carbon sink, on timescales longer than the calcium-compensation time in the ocean, carbonate weathering is either carbon-neutral or is a carbon source where dissolution occurs via sulfuric acid.

Existing weathering models based on silicate-rich settings are typically parameterized as supply-limited for lower denudation rates, where weathering and erosion are coupled, and kinetically limited at faster denudation rates, where weathering and erosion are decoupled (West et al., 2005). In contrast, because of more rapid kinetics, carbonate weathering is unlikely to be kinetically limited and, instead, is either limited by the supply of fresh rock or by the availability of acid (primarily carbonic acid) that can dissolve carbonate rock (Calmels et al., 2011; Gaillardet et al., 2018; Romero-Mujalli et al., 2018). The supply of acid is controlled by a number of factors, including temperature, the efficiency of soil respiration that supplies $CO_2$ for carbonic acid to the bedrock, and the oxidation of sulfates that creates sulfuric acid. Both the total $CO_2$ available for weathering and the temperature control the saturation of the solution with respect to calcite (Drake and Wigley, 1975). Thus, for undersaturated fluids, carbonate weathering may be strongly coupled with erosion, whereas it becomes decoupled from erosion

and coupled to acid availability, once saturation is achieved. As a consequence, the mechanisms that control how denudation is partitioned in a dominantly carbonate orogen may differ substantially from those that control denudation partitioning in silicate orogens (Gaillardet et al., 2018; Ott et al., 2019).

Young orogens in particular often expose marine sedimentary sequences that can host significant volumes of carbonate, either as massive carbonate terranes or interbedded with siliciclastic sediments. For example, the entire Alpine-Zagros-Himalayan orogenic complex has a common genesis during the Mesozoic, when carbonate platforms covered a large area of the Tethys Ocean. These carbonates have been subsequently uplifted during the ongoing closure of the Tethys Ocean in the Cenozoic (Dercourt and Vrielynck, 1993; Philip et al., 1996). Yet, because such ranges are poorly represented in existing studies, we lack the ability to understand how uplift of such ranges may impact biogeochemical cycling and sediment budgets. Indeed, cooling during the Cenozoic is frequently attributed to the uplift of mountains, but if the majority of active ranges in the Cenozoic are comprised of carbonate-rich bedrock, the mechanistic coupling between mountain uplift and cooling—and subsequent impact on the carbon cycle—may require revision.

In this paper, we investigate the partitioning of physical and chemical denudation between carbonates and silicates in a carbonate-rich orogen, the Northern Apennines (Figure 1). To this end, we use existing $^{10}$Be catchment-averaged denudation rates (Cyr and Granger, 2008; Cyr et al., 2014; Wittmann et al., 2016; Erlanger, 2020), riverine dissolved solutes, and the fraction of carbonate sand in river sediment in 18 individual catchments draining the Northern Apennines. The results from this study reveal four key characteristics of denudation partitioning: (1) physical erosion dominates the total denudation flux in the Northern Apennines, and the relative contribution of carbonates and silicates to the physical erosion flux appears to be lithologically controlled, (2) denudation fluxes are decoupled from both silicate and carbonate weathering, likely due to kinetic limitations on silicate weathering and acid-supply limits on carbonate weathering, (3) the carbonate weathering flux is greater than the silicate weathering flux, and (4) in carbonate-rich catchments, up to 90% of dissolved $Ca^{2+}$ ions are precipitated as secondary

144 calcite, an important process that converts chemically mobilized solutes back into solid grains
145 that can once again be transported physically.

146

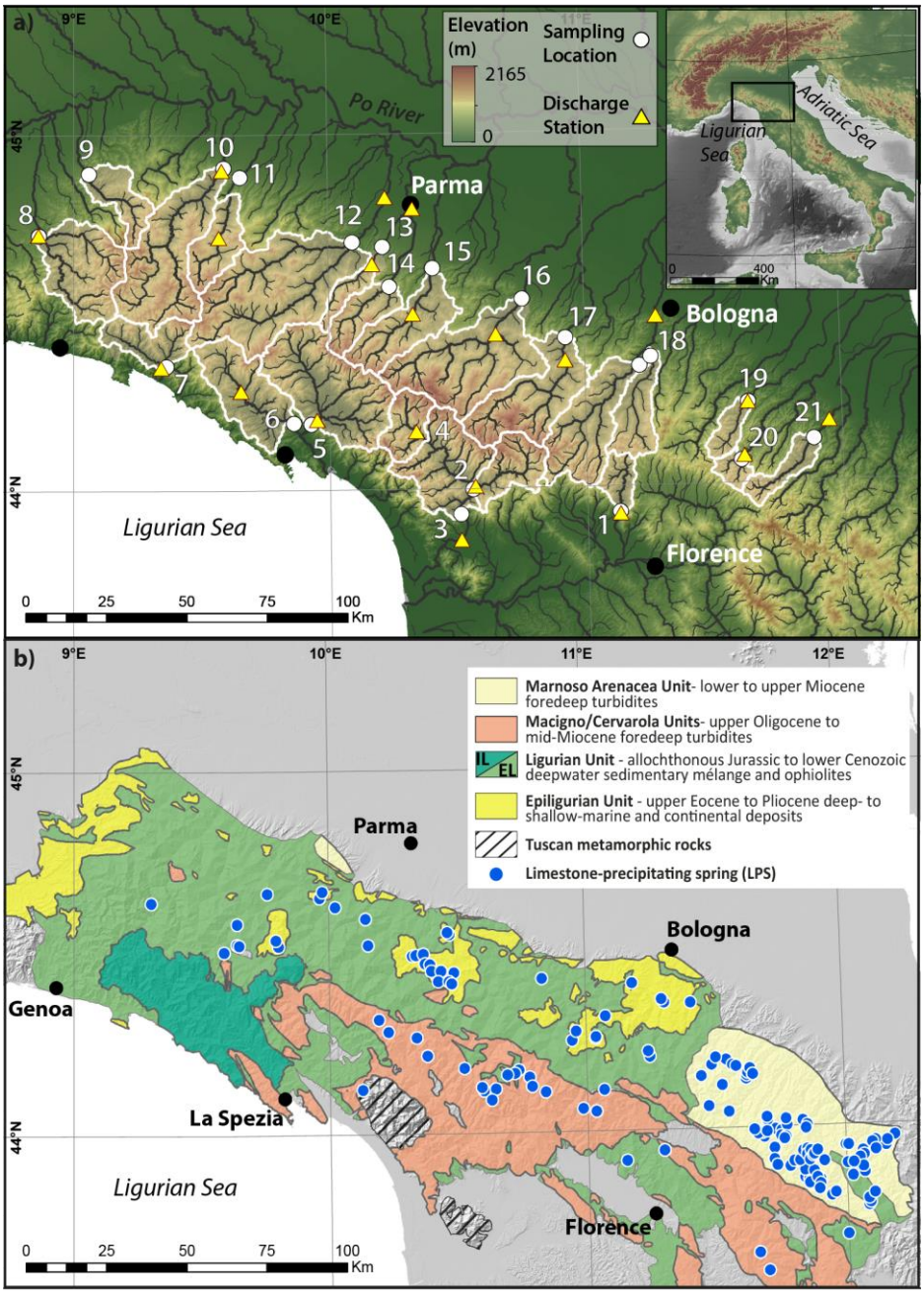


147
148 **Figure 1**. a) Overview map with locations of sampled sediment and water (white circles) and
149 discharge stations (yellow triangles). White polygons illustrate the sampled catchment area for
150 sediment and water samples, and numbers correspond to catchment names given in all
151 manuscript tables. b) Geologic map of the Northern Apennines. The Ligurian Unit is divided into
152 the Internal Ligurian Unit (IL; dark green) and the External Ligurian Unit (EL; light green). Gray

areas are not mapped and white area represents the Ligurian Sea. Limestone-precipitating springs mapped by Cantonati et al. (2016) and Segadelli and De Nardo (2018) are shown as blue dots.

## 2 Setting

### 2.1 Geology

The Northern Apennines form part of the Alpine orogenic belt and were uplifted and sub-aerially exposed by ~4–5 Ma (Le Pichon et al., 1971; Fellin et al., 2007). This mountain range is a type example for the initial stages of orogenesis, characterized by an intact sedimentary cover of mixed siliciclastic-carbonate lithologies, with little to no metamorphic rocks and relatively low relief. Lithologies exposed in the Northern Apennines are dominated by marine sedimentary sequences deposited as turbidites (Tertiary Foredeep units), which are divided into the Macigno, Cervarola, and Marnoso Arenacea Units (Figure 1b). Overlying these deposits are remnants of the Ligurian Tethys Ocean (Ligurian Unit), comprised of pelagic successions and turbidites (Vai and Martini, 2001). The Ligurian Unit is subdivided into (1) the External Ligurian Unit (EL), which consists of clayey shales, carbonaceous and siliciclastic turbidites, and (2) the Internal Ligurian Unit, which consists of pelagic limestone, sandstone, and minor ophiolites (Ricci Lucchi, 1986; Molli, 2008). Overlying the EL, mixed siliciclastic and carbonate deposits formed in perched basins from the mid-Eocene to the Pliocene, and comprise the so-called Epi-Ligurian Unit.

We refer to the northeast flank of the mountain range as the Adriatic side, where all rivers drain into the Po Plain and ultimately to the Adriatic Sea, and refer to the southwest flank as the Ligurian side, where rivers drain into the Ligurian Sea (Figure 1a). On the Adriatic side, limestone-precipitating springs (LPS) have been mapped mostly in the Tertiary Foredeep and Epi-Ligurian units (Figure 1b) and are associated either with perched, isolated aquifers formed from slope-gravitational movements, or with aquifers formed along fault planes (Cantonati et al., 2016). Other LPS have been observed in the Ligurian Units and are also associated with gravitational processes (i.e. landslides) that are a common occurrence in these lithologies (Carlini et al., 2016; Segadelli et al., 2017).

### 2.2 Climate

The climate in the Northern Apennines is characterized as Mediterranean, with average temperatures of ~10°C. Average January temperatures are 0°C in the mountains and up to 10°C on the Ligurian coastlines, compared with a more spatially consistent July average of 15–20°C (Brunetti et al., 2014). Precipitation primarily falls as snow or winter rain, with a maximum (300–800 mm) during the months of September through February, and a minimum (150–300 mm) during the months of June through August (Crespi et al., 2018). During the fall, winter, and spring, precipitation is approximately a factor of 2 higher on the Ligurian side and in the highest elevations on the Adriatic side, relative to the middle and lower reaches of catchments on the Adriatic side (Crespi et al., 2018). During the summer months (June, July and August), seasonal precipitation is similar across the divide (250-350 mm) in the Northern Apennines (Crespi et al., 2018).

Maximum river discharge occurs during the months of November to March. Average annual runoff (discharge divided by upstream catchment area) compiled for each studied catchment over the last five available years is ~1.2–2.2 m/yr along Ligurian rivers. Runoff and denudation typically illustrate a positive correlation (Summerfield and Hulton, 1994), although catchment-averaged denudation rates and runoff from Northern Apennine rivers appear to be negatively correlated (Figure S1).

## 3 Materials and Methods

### 3.1 Water Chemistry

In order to quantify chemical weathering and physical erosion fluxes, we collected water samples and sediment samples from the Northern Apennines. For the water samples, we measured solute concentrations, which are multiplied with estimated river runoff to obtain weathering fluxes. We sampled sediment from active channels and overbank deposits during two sampling seasons in March and July of 2018. These two months broadly correspond to the times of yearly minimum and maximum runoff and were chosen to bracket as much as possible the yearly range of streamflow conditions. Sampling sites were chosen near locations with existing constraints on catchment-averaged denudation rates (Figure 1a). Additionally, over the course of four sampling campaigns (May 2017, July 2017, March 2018, and July 2018), we collected three 30 mL bottles

of river water at each sample location. All water samples were filtered through 0.2 μm VWR filters. Cation samples were acidified with laboratory-grade HCl to a pH of 2 or lower, and all samples were kept cool and away from light until analysis. Alkalinity was measured in the field (maximum 24 hours after collection) for most samples using either end-point or Gran titration techniques with a Hach digital titrator. Cation concentrations of water samples were analyzed on a Thermo-Fischer Element XR sector-field inductively-coupled-plasma (ICP) mass spectrometer. Concentrations were then calculated from the measured intensities, using a single-point calibration compared with an in-house primary standard. In-house standards were calibrated with the Certified Reference Standards of DIONEX. The National Research Council of Canada river standard SLRS-6 and NIST 1640 secondary multi-element standards were used to assess the accuracy and precision of these measurements. Standards solute concentrations agree with certified values to within 5–10%, and 2σ uncertainties for replicate analyses of the standards were less than 7%.

Anion concentrations and cation replicates were analyzed on a Dionex DX-120 ion chromatography (IC) instrument, with an IonPac AS14, 4 x 250 mm column and an ASRIS-Ultra Suppressor with AutoSuppression. To prepare all eluents of $NaCO_3$, deionized water (with a resistance of higher than 18.2 MΩ) from a Milli-Q water unit was used. For all anions and cations, analytical uncertainties were below 5%.

### 3.2 Catchment-Averaged Denudation Rates

Detrital, catchment-averaged denudation rates derived from $^{10}Be$ concentrations were compiled from catchments around the Northern Apennines (Cyr and Granger, 2008; Cyr et al., 2014; Wittmann et al., 2016; Erlanger, 2020). Due to the fact that these samples were collected over different years and assume different cosmogenic nuclide scaling schemes to calculate denudation rates, we use the denudation rates given in Erlanger (2020), which includes rates from other studies (Cyr and Granger, 2008; Cyr et al., 2014; Wittmann et al., 2016) that were recalculated using the method of Lupker et al. (2012). All denudation rates were then converted to fluxes using a quartz density of 2.65 g/cm$^3$.

### 3.3 Carbonate Sand

Sediment samples were cleaned to remove organic matter and sieved to obtain the 250–500 μm fraction. We used grain sizes within the range of the $^{10}$Be denudation rates (125–700 μm), in order to avoid potential grain size bias when comparing silicate and carbonate weathering and erosion fluxes. Approximately 50 g of sand (or the available mass) was weighed and dissolved in HCl. The remaining mass was rinsed, dried, and weighed. The difference between the original and final mass was assumed to represent the percent carbonate within the sand-sized fraction.

### 3.4. Water Solute Corrections and Calculations

For some catchments, we collected a repeat sample from the same location during both the winter and summer season. Where appropriate, when we discuss results from one of the repeat measurements, we refer to an individual "sample". When the collective set of sample(s) from a catchment are discussed, we refer to the "catchment".

Solute concentrations were initially corrected to account for rainwater inputs. We additionally assess the saturation state of the samples with respect to calcite, because the widespread presence of travertine deposits and limestone-precipitating springs in the Northern Apennines (Figure 1b) (Cantonati et al., 2016; Segadelli and de Nardo, 2018) suggests that waters in many catchments may be oversaturated with respect to calcite.

#### 3.4.1 Cyclic Inputs

We corrected our solute concentrations for rainwater inputs using atmospheric $Cl^-$ as an index for atmospheric inputs to rivers. For large rivers that integrate sizable catchments, water chemistry data suggest that atmospheric $Cl^-$ concentrations should be lower than 30 μmol/L (Gaillardet et al., 1999). Due to the proximity of the Northern Apennines to the Ligurian and Adriatic Seas, the seawater contribution of $Cl^-$ may be higher than 30 μmol/L. The lowest measured $Cl^-$ concentration is 64.6 μmol/L. We assume that this value is representative of the rainwater contribution to all rivers and correct major dissolved species for rainwater inputs using the stoichiometry of seawater. For sulfate, we assume that sulfate-chloride ratios in rain are twice as high as in seawater, following Stallard and Edmond (1981).

#### 3.4.2 Saturation Index

The saturation index (SI) of a solution is defined as (Langmuir, 1971):

$$SI_{calcite} = \log(IAP_{calcite}/K_{calcite}) \quad (1)$$

$$IAP_{calcite} = a_{Ca} \cdot a_{HCO_3} \cdot K_2/10^{-pH} \quad (2)$$

where IAP is the ionic activity product, $K_{calcite}$ is the equilibrium constant for carbonate, $a_{Ca}$ and $a_{HCO3}$ are the activities of $Ca^{2+}$ and $HCO_3^-$ (Davies and Shedlovsky, 1964), and $K_2$ is the second dissociation constant of $H_2CO_3$. Here, we assume that the concentrations of $Ca^{2+}$ and $HCO_3^-$ are equal to the activities.

### 3.5 Calculation of denudation fluxes

Denudation, weathering, and physical erosion fluxes were calculated for 25 samples from 18 catchments. We excluded samples from these calculations due to unavailable carbonate sand measurements (River No. 4); unavailable discharge data (River No. 9); unavailable denudation measurements (Cutigliano sample from River No. 2 and the Castello di Sambuca from River No. 18); textile pollution in River No. 1, based on elevated Na+ and $SO_4^{2-}$ (Cortecci et al., 2002), for which we cannot confidently correct; or to "contamination" by evaporite weathering (Text S1), based on mapped distributions of evaporites in these catchments,.

For silicate weathering, the contribution of major dissolved ions was calculated by summing the concentrations of the following species, expressed as major cations and silicon derived from silicate rocks (expressed in $kg/m^3$ or g/L):

$$TDS_{sil} = [Ca^{2+}]_{Sil} + [Mg^{2+}]_{Sil} + [Na^+]_{Sil} + [K^+]_{Sil} + [Si] \quad (3)$$

Here, the square brackets designate concentrations. We refer to this quantity as "silicate dissolved solids" ($TDS_{Sil}$). Because $Ca^{2+}$ and $Mg^{2+}$ can be derived from both carbonate and silicate weathering, we partitioned the concentrations based on molar ratios from a global compilation of streams draining pure silicate lithologies $Ca_{sil}/Na$ (0.35) and $Mg_{sil}/Na$ (0.24) (Gaillardet et al., 1999). In the absence of local constraints, this global silicate endmember appears to be a fair approximation of the local endmember in the Northern Apennines (Figure

S3). Furthermore, we find no local lithological data which supports the use of a single endmember for the entire group of data (Figure S3).

The silicate chemical weathering flux (in t/km$^2$/yr) is calculated using the following equation:

$$W_{Sil} = \frac{Q_{riv} * TDS_{Sil}}{A_{riv}} = \frac{Q_{riv}}{A_{riv}} * \left( M_{Na} * [Na^+]_{sil} + M_K * [K^+]_{sil} + M_{Mg} * [Mg^{2+}]_{sil} + M_{Ca} * [Ca^{2+}]_{sil} + M_{Si} * [Si] \right) \quad (4)$$

where $M_x$ is the molar mass (g/mol) of element X, and $Q_{riv}/A_{riv}$ is the runoff, expressed as the time-integrated water discharge (m$^3$/y) divided by the upstream drainage area (m$^2$).

For carbonate weathering, the concentrations of $Ca^{2+}_{carb}$ and $Mg^{2+}_{carb}$ are assumed to be the difference between the total concentrations and the silicate contribution. We define the "carbonate dissolved solids" ($TDS_{Carb}$) as:

$$TDS_{carb} = [Ca^{2+}]_{Carb} + [Mg^{2+}]_{Carb} = ( [Ca^{2+}]_{Total} + [Mg^{2+}]_{Total}) - ([Ca^{2+}]_{Sil} + [Mg^{2+}]_{Sil}) \quad (5)$$

The carbonate weathering flux ($W_{Carb}$) is then calculated using equation 6:

$$W_{Carb} = \frac{Q_{riv} * TDS_{Carb}}{A_{riv}} = \frac{Q_{riv}}{A_{riv}} * \left( M_{Mg} * [Mg^{2+}]_{Carb} + M_{Ca} * [Ca^{2+}]_{Carb} \right) \quad (6)$$

The total denudation flux (D) is defined as the sum of chemical weathering fluxes ($W_{Carb}$ + $W_{Sil}$) and the physical erosion flux (E) (Equation 7). Although $^{10}$Be denudation rates record the exhumation of quartz grains, we assume that these rates reflect the lowering rate over the entire catchment, and thereby apply to both siliciclastic and carbonate lithologies. In the Northern Apennines, carbonates occur both interbedded with and as accessory minerals within siliciclastic lithologies, and no steep carbonate cliffs or large areas that drain exclusively quartz or carbonate lithologies are reported here. We also assume that the sand fraction—and the fraction of silicate and carbonate within this fraction—represent the partitioning of erosion between silicates and

carbonates. We thus refer to the erosional flux within the sand-sized fraction as the "total physical erosion", which is expressed as:

$$E_{total}=D - (W_{sil}+ W_{carb}) \quad (7)$$

To partition the physical erosion flux into carbonates and silicates, we use the percent carbonate sand determined for each river to obtain the carbonate erosion flux:

$$E_{carb}=E_{total} * \%Sand_{carb} \quad (8)$$

and:

$$E_{sil}=E_{total} - E_{carb} \quad (9)$$

We propagate uncertainties of all quantities from the analytical and reported uncertainties of the underlying measurements.

## 4 Results

### 4.1 Carbonate Sand

Catchment-wide percent carbonate sand varies from 17–76% (Figure 2, Table S1) and values observed here are consistent with point counts of lithic carbonate sand grains (Lc) observed in these catchments (Garzanti et al., 1998, 2002) (Table S1). Catchments that exclusively drain the same geologic unit have similar percent carbonate sand. For example, the carbonate content of catchments draining the Internal Ligurian Unit (6–7) ranges from 17–18%; catchments draining the Macigno/Cervarola Unit (1–3), 20–28%; catchments draining the Marnoso Arenacea (19–21), 21–42%, and; catchments draining the EL (9–10 and 12–13), 60–76%. Sampled catchments that drain a mixture of units generally have carbonate sand percentages outside the range of those that exclusively drain one lithology (Figures 1–2). We also find a strong positive correlation ($R^2$ = 0.82) between the percent carbonate sand and the areal exposure of the EL within a catchment (Figure 3).

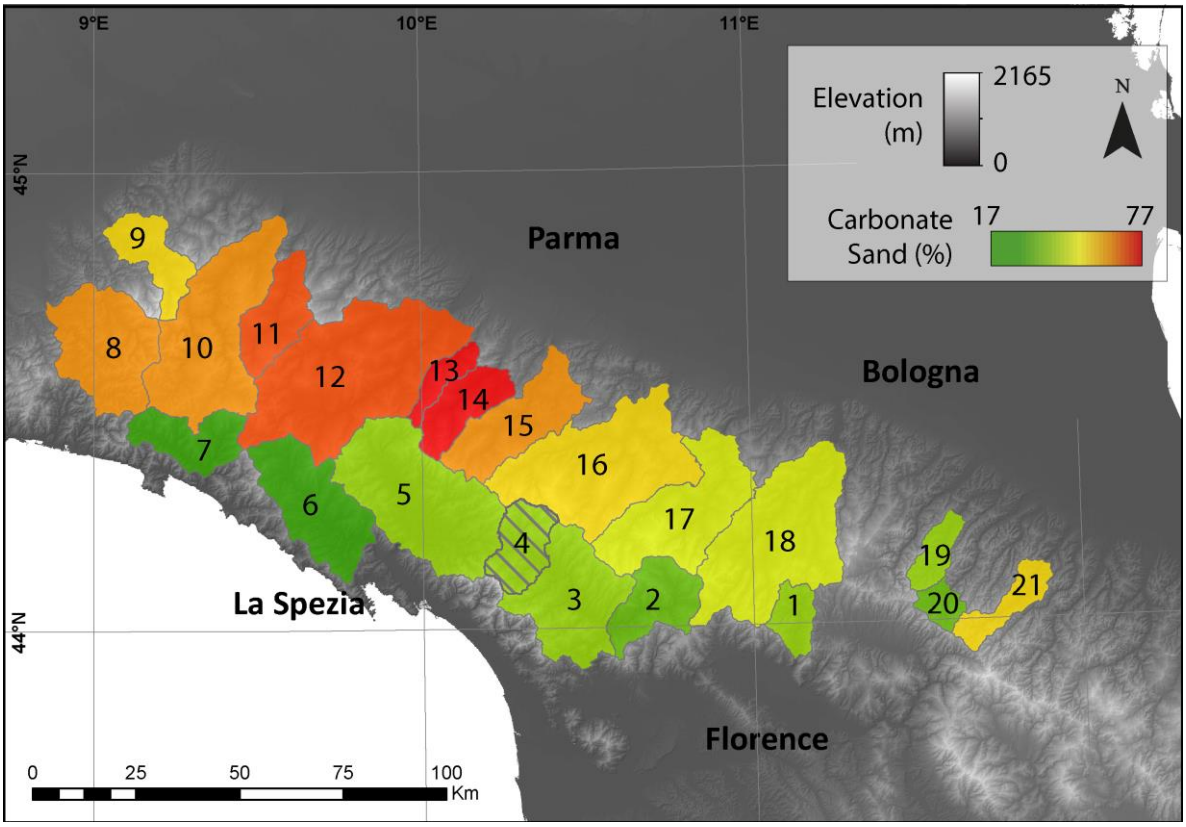


**Figure 2**. Percent carbonate sand for each catchment. Numbers correspond to catchment numbers in Table S1. The hatched pattern corresponds to River No. 4, for which data were not available. The light green color beneath the hatched pattern corresponds to River No. 3, which encompasses River No. 2 and 4.

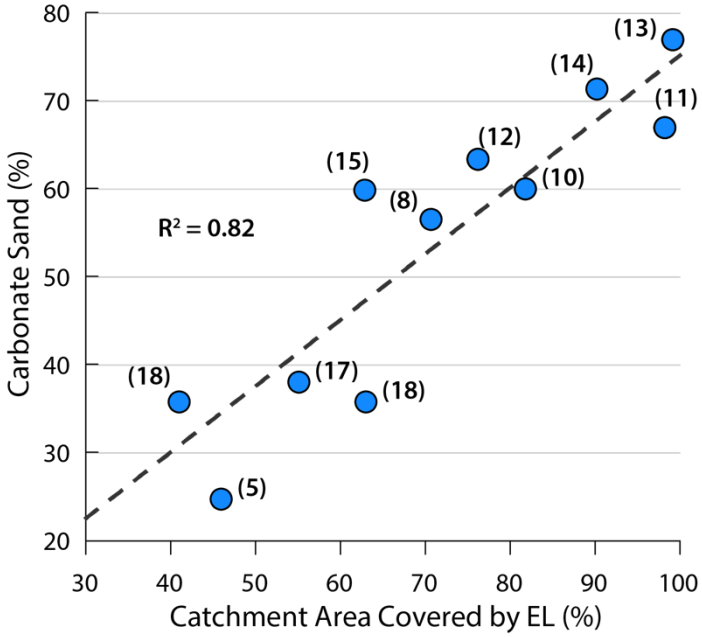


**Figure 3.** Catchment area that exposes the EL plotted against percent carbonate sand. Numbers in parentheses indicate the river number as shown in Figure 1a.

### 4.2 Solutes

Riverine samples from the Northern Apennines are slightly alkaline, with pH values ranging from 7.7–9.1, and major dissolved ion concentrations that are dominated by $Ca^{2+}$ and $HCO_3^-$ (Table S2). Most catchments have SI values greater than zero (Figure 4, Table S3), which indicates that the waters are oversaturated with respect to calcite. The lowest SI values (<0) reflect undersaturated conditions and are sourced exclusively from catchments on the Ligurian side of the drainage divide.

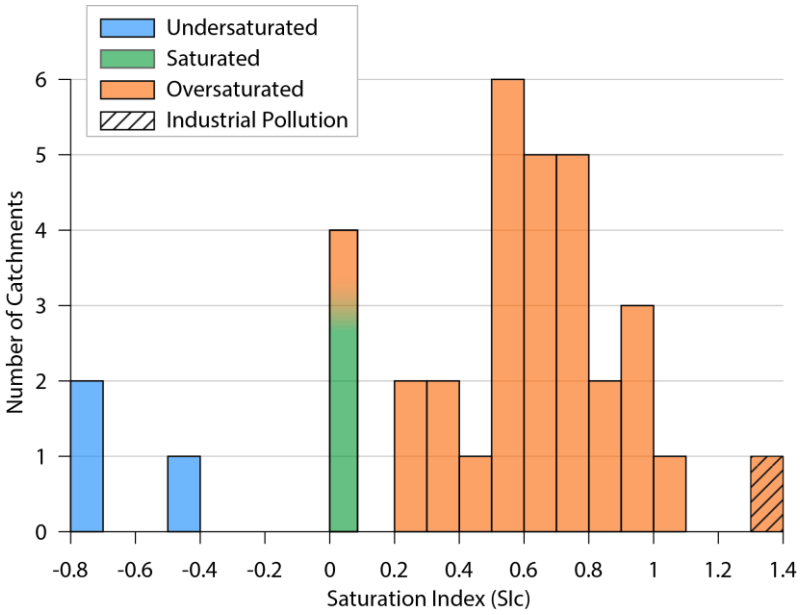


**Figure 4**. Histogram of saturation index results. Undersaturated samples (blue bars) have values below zero, saturated samples (green bar) are at saturation, and oversaturated samples (orange bars) have values above zero. The hatched pattern refers to the River No. 1, which is affected by pollution from nearby textile industries (Cortecci et al., 2002) and produced high ion concentrations that could not be attributed to natural sources.

### 4.3 Erosion and Weathering Fluxes

Total denudation fluxes derived from $^{10}Be$ concentrations vary over an order of magnitude, from 278–2226 t/km$^2$/yr (Table 1). Total physical erosion fluxes ($E_{Total}$) range from 121–2151 t/km$^2$/yr. Partitioned into carbonate physical erosion ($E_{Carb}$) and silicate physical erosion ($E_{Sil}$), the ratio of $E_{Carb}/E_{Sil}$ varies from 0.21–3.35, where 52% of samples have higher $E_{Sil}$ fluxes than $E_{Carb}$ fluxes (Table 1).

Total weathering fluxes ($W_{Total}$) vary from 38–165 t/km$^2$/yr (Table 1). $E_{Total}/W_{Total}$ is 24.0 on average, illustrating that physical erosion fluxes generally exceed chemical weathering fluxes by up to an order of magnitude. Carbonate weathering fluxes ($W_{Carb}$ = 19–93 t/km$^2$/yr) are higher than the silicate weathering fluxes ($W_{sil}$ = 9–72 t/km$^2$/yr). The ratio of $W_{Carb}/W_{Sil}$ varies from 0.95– 4.77, and is greater than 1 for all catchments, except River No. 19. The average ratio of $W_{Carb}/W_{Sil}$ = 2.35, illustrating that carbonate weathering fluxes are on average a factor of 2 higher than silicate weathering fluxes.

**Table 1.** Denudation fluxes, physical erosion fluxes, and chemical. weathering fluxes.

| Catchment Number | Catchment Name | Sample Number | Latitude | Longitude | Sampling Date | D ($t/km^2/yr$) | $W_{Total}$ ($t/km^2/yr$) | $W_{Carb}$ ($t/km^2/yr$) | $W_{Sil}$ ($t/km^2/yr$) | $E_{Total}$ ($t/km^2/yr$) | $E_{Carb}$ ($t/km^2/yr$) | $E_{Sil}$ ($t/km^2/yr$) | Annual Runoff (m/yr) | $W_{Total}/E_{Total}$ | $E_{carb}/E_{sil}$ |
|---|---|---|---|---|---|---|---|---|---|---|---|---|---|---|---|
| 2 | Lima | 1 | 43.999° | 10.554° | 15.07.18 | 504 ± 58 | 83 ± 10 | 61.6 ± 10 | 21.6 ± 0.5 | 420 ± 59 | 84 ± 59 | 336 ± 84 | 1.23 | 5.05 | 0.25 |
| 4 | Serchio | 1 | 44.137° | 10.374° | 15.07.18 | 511 ± 69 | 49 ± 5 | 42.3 ± 5 | 7.2 ± 0.2 | 462 ± 64 | | | 0.57 | 9.34 | ND |
| 5 | Magra | 1 | 44.187° | 9.926° | 20.03.18 | 572 ± 85 | 62 ± 5 | 43.8 ± 5 | 17.8 ± 0.4 | 511 ± 85 | 126 ± 85 | 384 ± 120 | 0.94 | 8.29 | 0.33 |
| 6 | Vara | 1 | 44.192° | 9.858° | 20.03.18 | 278 ± 42 | 57 ± 6 | 42.5 ± 6 | 14.5 ± 0.3 | 221 ± 36 | 41 ± 36 | 181 ± 51 | 1.47 | 3.89 | 0.23 |
| 6 | Vara | 2 | 44.190° | 9.858° | 15.07.18 | 278 ± 42 | 100 ± 14 | 75.4 ± 14 | 24.5 ± 0.6 | 178 ± 29 | 33 ± 29 | 145 ± 41 | 1.47 | 1.79 | 0.23 |
| 7 | Entella | 1 | 44.351° | 9.362° | 20.03.18 | 286 ± 34 | 89 ± 9 | 69.9 ± 9 | 19.2 ± 0.5 | 197 ± 36 | 34 ± 36 | 163 ± 50 | 2.17 | 2.21 | 0.21 |
| 7 | Entella | 2 | 44.351° | 9.362° | 15.07.18 | 286 ± 34 | 158 ± 16 | 92.7 ± 16 | 65.2 ± 1.6 | 128 ± 38 | 22 ± 38 | 106 ± 54 | 2.17 | 0.81 | 0.21 |
| 8 | Scrivia | 1 | 44.719° | 8.860° | 18.03.18 | 710 ± 126 | 47 ± 4 | 38.3 ± 4 | 8.7 ± 0.2 | 663 ± 122 | 375 ± 122 | 288 ± 173 | 0.58 | 14.11 | 1.30 |
| 10 | Trebbia | 1 | 44.908° | 9.590° | 22.03.18 | 1171 ± 594 | 63 ± 7 | 51.4 ± 7 | 11.2 ± 0.3 | 1109 ± 586 | 666 ± 586 | 443 ± 829 | 0.82 | 17.72 | 1.50 |
| 10 | Trebbia | 2 | 44.909° | 9.589° | 15.07.18 | 1171 ± 594 | 76 ± 10 | 41.2 ± 10 | 34.4 ± 0.8 | 203 ± 32 | 122 ± 32 | 81 ± 45 | 0.82 | 2.68 | 1.50 |
| 11 | Nure | 1 | 44.882° | 9.653° | 21.03.18 | 1063 ± 193 | 86 ± 15 | 65.2 ± 15 | 21.3 ± 0.5 | 976 ± 194 | 654 ± 194 | 322 ± 274 | 0.78 | 11.29 | 2.03 |
| 11 | Nure | 1 | 44.828° | 9.617° | 15.07.18 | 1063 ± 193 | 73 ± 15 | 54.5 ± 15 | 18.3 ± 0.5 | 990 ± 194 | 663 ± 194 | 327 ± 274 | 0.78 | 13.60 | 2.03 |
| 12 | Taro | 1 | 44.698° | 10.093° | 21.03.18 | 1598 ± 326 | 71 ± 10 | 58.5 ± 10 | 12.1 ± 0.3 | 1527 ± 316 | 968 ± 316 | 559 ± 447 | 0.84 | 21.63 | 1.73 |
| 12 | Taro | 2 | 44.697° | 10.094° | 15.07.18 | 1598 ± 326 | 75 ± 12 | 53.0 ± 12 | 21.5 ± 0.5 | 1523 ± 314 | 966 ± 314 | 558 ± 444 | 0.84 | 20.44 | 1.73 |
| 13 | Baganza | 2 | 44.606° | 10.123° | 15.07.18 | 726 ± 289 | 59 ± 9 | 36.8 ± 9 | 22.5 ± 0.5 | 667 ± 289 | 513 ± 289 | 153 ± 409 | 0.71 | 11.24 | 3.35 |
| 13 | Baganza | 1 | 44.605° | 10.120° | 21.03.18 | 726 ± 289 | 71 ± 8 | 60.1 ± 8 | 10.7 ± 0.3 | 655 ± 289 | 505 ± 289 | 151 ± 409 | 0.71 | 9.25 | 3.35 |
| 14 | Parma | 1 | 44.569° | 10.237° | 15.07.18 | 1140 ± 201 | 85 ± 12 | 52.8 ± 12 | 32.6 ± 0.8 | 1054 ± 190 | 753 ± 190 | 302 ± 268 | 1.01 | 12.34 | 2.50 |
| 15 | Enza | 1 | 44.627° | 10.413° | 15.07.18 | 1317 ± 329 | 96 ± 14 | 57.0 ± 14 | 39.5 ± 1.0 | 1221 ± 329 | 731 ± 329 | 490 ± 465 | 0.97 | 12.66 | 1.49 |
| 17 | Panaro | 1 | 44.420° | 10.925° | 04.07.17 | 790 ± 121 | 67 ± 9 | 44.9 ± 9 | 22.0 ± 0.5 | 723 ± 111 | 275 ± 111 | 448 ± 157 | 0.78 | 10.80 | 0.61 |
| 18 | Reno | 1 | 44.338° | 11.213° | 01.05.17 | 1540 ± 305 | 47 ± 6 | 33.4 ± 6 | 13.3 ± 0.3 | 1493 ± 299 | 535 ± 299 | 958 ± 423 | 0.67 | 32.01 | 0.56 |
| 18 | Reno | 1 | 44.362° | 11.257° | 03.05.17 | 2226 ± 925 | 73 ± 9 | 39.8 ± 9 | 32.9 ± 0.8 | 2153 ± 916 | 771 ± 916 | 1382 ± 1295 | 0.67 | 29.63 | 0.56 |
| 19 | Senio | 1 | 44.227° | 11.632° | 15.07.18 | 1269 ± 265 | 66 ± 16 | 32.9 ± 16 | 32.9 ± 0.8 | 1204 ± 249 | 305 ± 249 | 899 ± 352 | 0.53 | 18.30 | 0.34 |
| 20 | Lamone | 1 | 44.065° | 11.601° | 15.07.18 | 822 ± 94 | 69 ± 14 | 45.8 ± 14 | 23.4 ± 0.6 | 752 ± 95 | 158 ± 95 | 594 ± 135 | 0.67 | 10.86 | 0.27 |
| 21 | Montone | 1 | 44.121° | 11.885° | 15.07.18 | 1545 ± 295 | 37 ± 8 | 19.4 ± 8 | 17.7 ± 0.4 | 1508 ± 296 | 639 ± 296 | 869 ± 418 | 0.32 | 40.59 | 0.74 |

D = Denudation flux (physical erosion + chemical weathering); $W_{Total}$ = Total Weathering Flux; $W_{Carb}$ = Carbonate Weathering Flux; $W_{Sil}$ = Silicate Weathering Flux; $E_{Total}$ = Total Physical Erosion flux; $E_{Carb}$ = Carbonate Physical Erosion Flux; $E_{Sil}$ = Silicate Physical Erosion Flux.

ND = Fluxes not determined for sample due to lack of carbonate sand measurements

### 4.4 Partition of Denudation between Carbonates and Silicates

Here, we compare denudation fluxes, total dissolved solids (TDS) as a proxy for chemical weathering, and the percent carbonate sand as a proxy for carbonate physical erosion. In each figure, we plot the entire set of samples, but differentiate between catchments draining the EL (gray circles), defined as catchments where the EL constitutes at least 50% of the exposed lithologies, from all other units (cyan circles). Additionally, we distinguish between oversaturated samples (solid pattern) and undersaturated/saturated samples ("x" pattern).

For catchments draining the EL, we find that percent carbonate sand does not scale with denudation fluxes (gray circles, Figure 5a). In turn, denudation fluxes illustrate a decoupling with carbonate dissolved solids, $TDS_{Carb}$, and only a weak correlation with silicate dissolved solids, $TDS_{Sil}$ ($R^2$=0.27), and total dissolved solids, $TDS_{Total}$ ($R^2$=0.34) (Figure 5b-d). However, we find a strong correlation, albeit with low significance (p=0.07) due to the small sample size, between carbonate weathering and denudation fluxes in all undersaturated/saturated samples (x pattern) ($R^2$=0.85) (Figure 5d). Similarly, $TDS_{Carb}$ and the percent carbonate sand are decoupled for oversaturated catchments (Figure 6) but illustrate a moderate correlation ($R^2$=0.71) for undersaturated samples (x pattern), although the significance is again low (p=0.16).

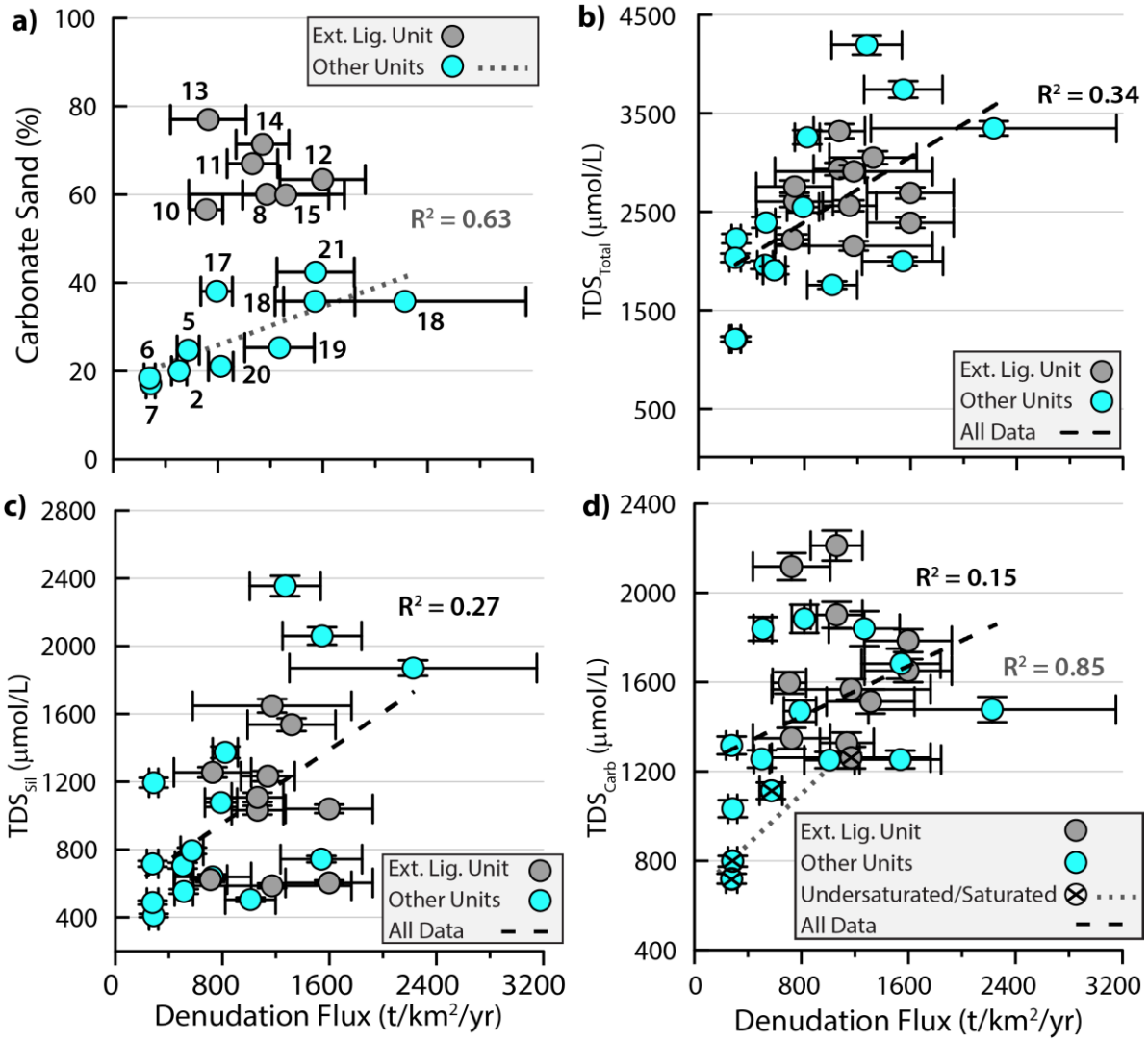


**Figure 5**. Denudation fluxes plotted against a) percent carbonate sand, b) $TDS_{Total}$ c) $TDS_{Sil}$, and d) $TDS_{Carb}$. EL samples (gray circles) are differentiated from Other Units (cyan circles). Dashed lines illustrate linear regressions for each full dataset with associated $R^2$ statistic. In a) dotted line refers only to samples from Other Units (cyan circles) ($R^2$=0.56), and numbers refer to catchments shown in Figure 1a. In d) solid circles illustrate oversaturated samples; undersaturated/saturated samples are overlaid with a "x". The dotted line ($R^2$=0.85) refers only to undersaturated/saturated samples.

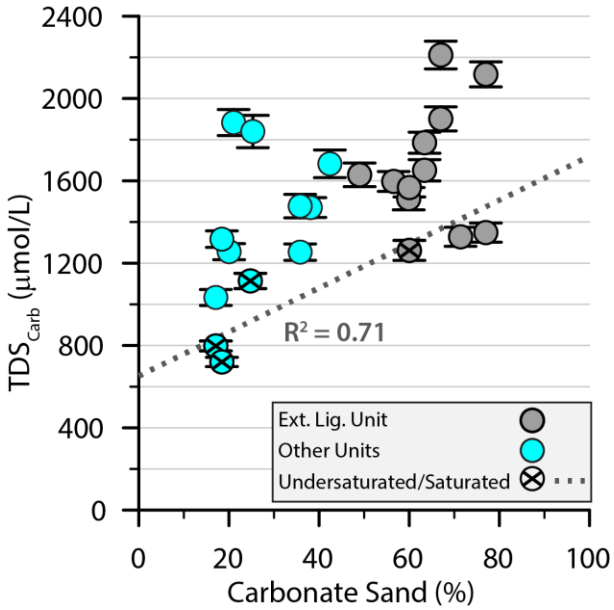


**Figure 6.** Percent carbonate sand plotted against $TDS_{Carb}$. The EL (gray circles) are distinguished from other lithologic units (red circles). Oversaturated samples are shown as solid circles; undersaturated and saturated samples are overlaid with a "x". Linear regressions and $R^2$ statistics are only shown for the undersaturated/saturated samples ($R^2$=0.71).

## 5 Discussion

In the following discussion, we investigate the mechanisms that control how denudation is partitioned between erosion and weathering and between carbonates and silicates and compare denudation and weathering fluxes from the Northern Apennines with a global data compilation from silicate-rich landscapes.

In the Northern Apennines, physical erosion is the dominant denudational process, and ratios of $E_{Carb}/E_{Sil}$ are variable, suggesting that both erosion of carbonates and silicates is important in this landscape (Table 1). However, we observe some important lithologic controls on carbonate erosion. In particular, the highest carbonate sand percentages (67–76%) are found in catchments exclusively draining the EL (Figure 2), and the percent carbonate sand and areal coverage by the EL illustrate a strong linear correlation (Figure 3), suggesting that the EL is the most important source of carbonate sand grains to river channels in the Northern Apennines.

However, we find no obvious lithologic control on the partitioning of chemical weathering and denudation (Figure 5b–d). Silicate and carbonate weathering fluxes (TDS x runoff) are uncorrelated with denudation, which could be explained by the negative correlation we observe between denudation and runoff (Figure S1). Along with the observed weak coupling or decoupling between weathering proxies and denudation fluxes, these findings are consistent

458 with a limitation for both silicate and carbonate weathering at erosion rates characteristic of the
459 Northern Apennines or higher. A kinetic limitation of silicate weathering rates has previously
460 been suggested for denudation rates >48 t/km$^2$/yr (West et al., 2005). Based on the widespread
461 oversaturation of sampled waters with respect to calcite, we suspect that carbonate weathering
462 rates are most likely limited by the availability of acid. As long as acid availability does not
463 increase with erosion rate, weathering rate and denudation should be decoupled, consistent with
464 our observations. The decoupling between carbonate weathering rate and denudation fluxes for
465 oversaturated samples and possible strong correlation with undersaturated/saturated samples
466 (Figure 5d) further supports the hypothesis that the carbonate weathering rate is not kinetically
467 limited, but is instead either limited by the supply of carbonates (undersaturated/saturated
468 samples) or the availability of acid (oversaturated samples).
469
470 **5.2 Global Comparison with Silicate-Rich Orogens**
471 Relative to other silicate-rich orogens with similar denudation fluxes (e.g. Eastern Southern Alps
472 of New Zealand, Colorado Rockies, Swiss Alps, and Andes Mountains), weathering fluxes (Text
473 S2) are generally higher in the Northern Apennines (red circles; Figure 7).

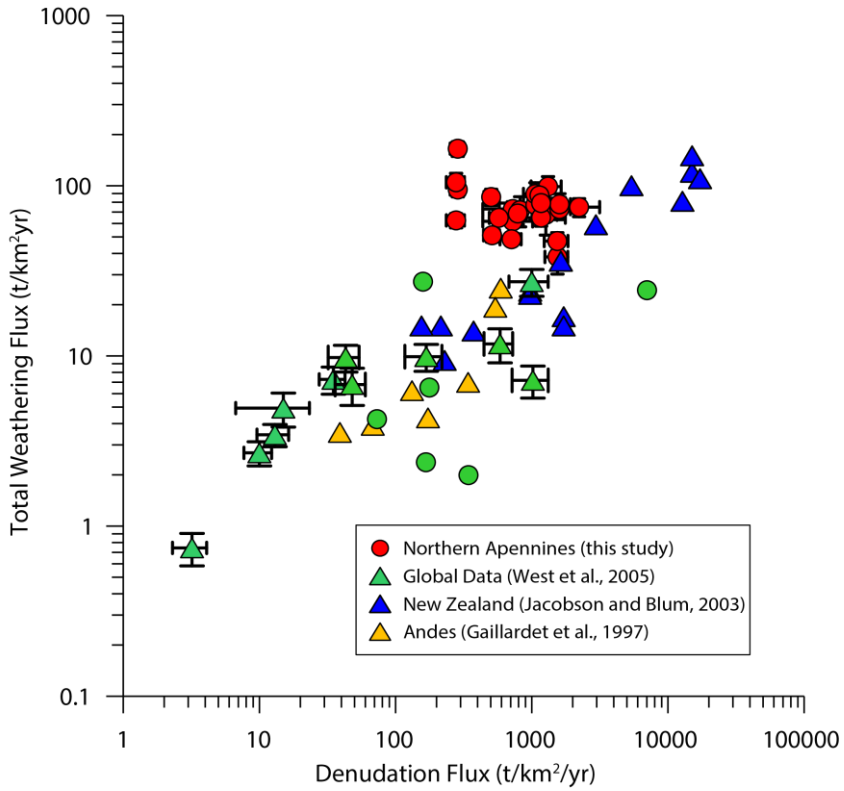


474

**Figure 7**. Northern Apennines denudation fluxes and total weathering fluxes plotted against a global data compilation. Triangles illustrate physical erosion fluxes derived from suspended sediment or average annual sediment fluxes, and circles illustrate denudation rates derived from cosmogenic nuclide data.

We compare our fluxes in more detail with those from the Eastern Southern Alps of New Zealand (ESA), as both regions are in temperate climates and weathering fluxes partitioned into carbonate and silicate components are also available for the Southern Alps (Jacobson and Blum, 2003). Physical erosion fluxes from the ESA (140–1700 t/km$^2$/yr) are similar to estimates from the Northern Apennines (129–2153 t/km$^2$/yr). However, the ratio of physical erosion to total weathering ($E_{Total}/W_{Total}$) in the ESA ranges from 9–150, with an average of 64, reflecting weathering fluxes that are 1–2 orders of magnitude lower than physical erosion fluxes. Average ratios of erosion to weathering fluxes ($E_{Total}/W_{Total}$ = 24.0) are lower in the Northern Apennines, reflecting the more important role of carbonate weathering in this setting. Carbonate weathering fluxes range from 8–100 t/km$^2$/yr in the ESA, compared with the range of 19–93 t/km$^2$/yr found in the Northern Apennines. Although the ESA are dominated by silicate-rich greywacke and schist lithologies with minor hydrothermal calcite veins, the ratio of carbonate to silicate weathering ($W_{Carb}/W_{Sil}$) is >1 for all except one sample, and has an average ratio of $W_{Carb}/W_{Sil}$ = 1.63. In the Northern Apennines, $W_{Carb}/W_{Sil}$ = 2.35—approximately a factor of 1.5 higher relative to the ESA— and we suggest that the difference in ratios between these two setting is due to lithologic differences. A lack of carbonate in stream sediments of the Southern Alps implies that carbonate weathering is likely supply-limited. In contrast, in the Northern Apennines, exported solutes from carbonate weathering appear to be limited by acid availability, rather than mineral supply. The current weathering state (i.e. the exported flux to rivers) in the Northern Apennines is thus one that is generally decoupled from mineral supply and entirely controlled by the kinetics of silicate dissolution (which modulates silicate weathering) and acid availability (which modulates carbonate weathering).

### 5.3 Limits on Weathering and Erosion in the Northern Apennines

#### 5.3.1 Secondary Calcite

As in carbonate-rich terranes globally, we observe that the vast majority of Northern Apennine waters are oversaturated with respect to calcite. When soil waters equilibrate at high $CO_2$ partial

pressures ($pCO_2$) in the subsurface and are discharged to streams, they begin to de-gas excess $CO_2$ to equilibrate with the lower atmospheric $pCO_2$. The resulting supersaturation of the waters with respect to the dissolved carbonates leads to the secondary precipitation of calcite (Bickle et al., 2015). The abundance of limestone-precipitating springs (Figure 1b) suggests that subsurface waters in the Northern Apennines are typically supersaturated in carbonates. Furthermore, we observe that a substantial fraction of the sand grains from the Lamone River are secondary carbonate sand grains (Figure S6), suggesting that precipitation and erosion of secondary carbonates is a major process in the Northern Apennines. Cavazza et al. (1993) similarly observed that up to 35% of the sand fraction in the Senio River (River No. 19) are such secondary carbonate "peloid" grains, comprised of organic material or quartz grains in the core and coated by a carbonate crust. Secondary calcite precipitation converts solutes back into rock that can be physically eroded—hence, it is a process that can potentially decouple the controls on weathering within the weathering zone from what is exported by rivers from the orogen. Further, by estimating the degree of secondary carbonate precipitation that occurred upstream of our sampling locations, we can quantify the flux of initially weathered material that has been subsequently converted back to solid grains and is no longer recorded in the flux of exported solutes in the river.

We estimate the proportion of secondary calcite precipitation in each lithology, adopting the procedures of Bickel et al. (2015) (Text S2). All quantities that include the inferred concentration of solutes lost to secondary precipitation are designated by an '*' (e.g. $TDS_{Total}$*) and are referred to as weathering zone fluxes. We use $\gamma$ to describe the proportion of calcium measured at our sampling location, relative to the inferred total calcium weathered from bedrock (Emberson et al., 2018). A value of $\gamma$=1 indicates that no secondary precipitation can be inferred from the chemical composition, and a value of $\gamma$=0 corresponds to the (hypothetical) situation in which all calcium was lost to secondary calcite precipitation. Oversaturated samples have average $\gamma$ values between 0.1–0.8, which indicates that between 20–90% of [$Ca^{2+}$] was lost to secondary calcite precipitation (Figure 9). Catchments draining the EL illustrate the largest offset between the solute regression line and bedrock regression line (Figure S4d), which results in the greatest corrections to [$Ca^{2+}$].

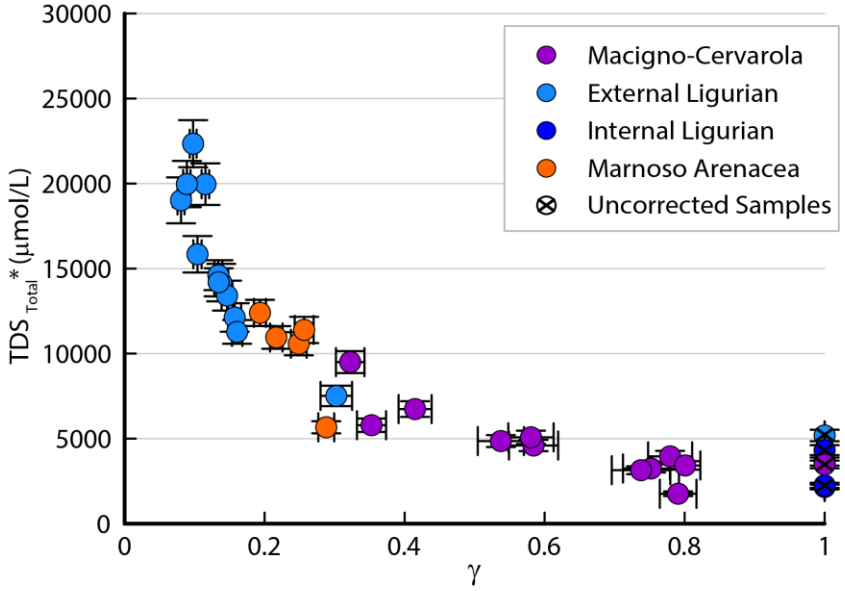


**Figure 9**. Results from secondary calcite precipitation calculations, showing γ plotted against $TDS_{Total}$* for major dissolved ions and trace elements, calculated with the adjusted [$Ca^{2+}$]. Samples with an "x" were not corrected for secondary calcite precipitation.

### 5.3.2 Weathering Zone Fluxes

Total weathering zones fluxes ($W_{Total}$*) vary from 63–602 t/$km^2$/yr (Table 2). The average ratio of total erosion fluxes to these weathering fluxes ($E_{Total}/W_{Total}$* = 4) is a factor of 6 lower relative to the average ratio for the exported fluxes ($E_{Total}/W_{Total}$ = 24).

Here, we illustrate the results in terms of the weathering zone total TDS concentrations ($TDS_{Total}$*) and weathering zone carbonate dissolved solids ($TDS_{Carb}$*). Note that the estimated concentrations from silicate dissolved solids ($TDS_{Sil}$) are unaffected by the correction for secondary calcite precipitation. $TDS_{Carb}$* constitutes 70–97% of $TDS_{Total}$*, and both measures are decoupled from denudation fluxes when considering the entire dataset (Figure 10a-b). Catchments draining the EL (gray circles) are characterized by the highest $TDS_{Total}$* values and are also decoupled from denudation. In turn, oversaturated samples from non-EL units illustrate a weak correlation between denudation and $TDS_{Total}$* ($R^2$=0.32, p=0.11) and $TDS_{Carb}$* ($R^2$=0.30, p=0.12) (Figure 10a-b). Finally, we observe a moderate correlation between $TDS_{Carb}$* and the percent catchment area covered by the EL ($R^2$=0.64) (Figure 10c) and the percent carbonate sand ($R^2$=0.66) (Figure 10d).

**Table 2.** Denudation fluxes, physical erosion fluxes, and chemical weathering fluxes adjusted for precipitation of secondary calcite.

| Name | Latitude | Longitude | Catchment Number | Sampling Date | D ($t/km^2/yr$) | $W_{total}$* ($t/km^2/yr$) | $W_{carb}$* ($t/km^2/yr$) | $W_{Sil}$ ($t/km^2/yr$) | $E_{Total}$* ($t/km^2/yr$) | $E_{carb}$* ($t/km^2/yr$) | $E_{Sil}$* ($t/km^2/yr$) | Average Annual Runoff (m/yr) | $W_{total}$*/$E_{Total}$* |
|---|---|---|---|---|---|---|---|---|---|---|---|---|---|
| Baganza | 44.6045° | 10.1202° | 13 | 15 07 2018 | 726.1 ± 288.9 | 498.2 ± 34.1 | 473.2 ± 34.1 | 25.0 ± 0.6 | 227.9 ± 290.9 | 175.4 ± 290.9 | 52.4 ± 411.3 | 0.71 | 8.01 |
| Baganza | 44.6061° | 10.1226° | 13 | 21 03 2018 | 726.1 ± 288.9 | 602.4 ± 35.0 | 589.6 ± 35.0 | 12.8 ± 0.3 | 123.7 ± 291.0 | 95.2 ± 291.0 | 28.4 ± 411.5 | 0.71 | 161.09 |
| Entella | 44.3509° | 9.3619° | 7 | 20 03 2018 | 286.2 ± 34.5 | 95.0 ± 9.0 | 69.9 ± 9.0 | 25.0 ± 0.6 | 191.2 ± 35.6 | 32.7 ± 35.6 | 158.5 ± 50.4 | 2.17 | 0.48 |
| Entella | 44.3513° | 9.3618° | 7 | 15 07 2018 | 286.2 ± 34.5 | 165.1 ± 16.4 | 92.7 ± 16.4 | 72.3 ± 1.6 | 121.1 ± 38.2 | 20.7 ± 38.2 | 100.4 ± 54.0 | 2.17 | 1.29 |
| Enza | 44.6267° | 10.4133° | 15 | 15 07 2018 | 1317.1 ± 328.6 | 483.1 ± 37.7 | 441.3 ± 37.7 | 41.9 ± 1.0 | 833.9 ± 330.8 | 499.4 ± 330.8 | 334.5 ± 467.8 | 0.97 | 0.47 |
| Lamone | 44.0651° | 11.6009° | 20 | 15 07 2018 | 821.5 ± 94.1 | 224.7 ± 17.5 | 198.9 ± 17.5 | 25.9 ± 0.6 | 596.8 ± 95.7 | 125.6 ± 95.7 | 471.2 ± 135.3 | 0.67 | 0.37 |
| Lima | 43.9993° | 10.5538° | 2 | 15 07 2018 | 503.5 ± 58.3 | 200.5 ± 13.8 | 176.3 ± 13.8 | 24.2 ± 0.6 | 303.0 ± 59.9 | 60.8 ± 59.9 | 242.2 ± 84.7 | 1.23 | 0.69 |
| Magra | 44.1869° | 9.9256° | 5 | 20 03 2018 | 572.4 ± 84.8 | 64.7 ± 5.0 | 43.8 ± 5.0 | 20.9 ± 0.5 | 507.7 ± 84.9 | 125.7 ± 84.9 | 382.0 ± 120.1 | 0.94 | 0.12 |
| Montone | 44.1210° | 11.8853° | 21 | 15 07 2018 | 1545.0 ± 295.5 | 121.1 ± 9.6 | 102.4 ± 9.6 | 18.7 ± 0.4 | 1423.8 ± 295.6 | 603.6 ± 295.6 | 820.2 ± 418.1 | 0.32 | 0.08 |
| Nure | 44.82832° | 9.6173° | 11 | 15 07 2018 | 1062.7 ± 193.5 | 359.0 ± 24.8 | 336.3 ± 24.8 | 22.7 ± 0.5 | 703.7 ± 195.0 | 471.5 ± 195.0 | 232.2 ± 275.8 | 0.78 | 0.41 |
| Nure | 44.8816° | 9.6532° | 11 | 21 03 2018 | 1062.7 ± 193.5 | 552.5 ± 32.6 | 528.3 ± 32.6 | 24.2 ± 0.6 | 510.2 ± 196.2 | 341.8 ± 196.2 | 168.4 ± 277.4 | 0.78 | 0.84 |
| Panaro | 44.41981° | 10.9245° | 17 | 15 07 2018 | 789.7 ± 120.6 | 174.4 ± 15.3 | 150.6 ± 15.3 | 23.8 ± 0.5 | 654.5 ± 109.3 | 249.1 ± 109.3 | 405.4 ± 154.5 | 0.78 | 0.12 |
| Parma | 44.5688° | 10.23709° | 14 | 15 07 2018 | 1139.5 ± 201.4 | 579.0 ± 37.4 | 544.2 ± 37.4 | 34.9 ± 0.8 | 560.5 ± 164.0 | 400.1 ± 164.0 | 160.3 ± 232.0 | 1.01 | 0.80 |
| Reno | 44.3380° | 11.2125° | 18 | 1 05 2017 | 1539.7 ± 304.8 | 76.6 ± 6.7 | 62.7 ± 6.7 | 14.0 ± 0.3 | 1463.0 ± 298.0 | 523.9 ± 298.0 | 939.2 ± 421.5 | 0.67 | 0.11 |
| Reno | 44.3622° | 11.2573° | 18 | 3 05 2017 | 2226.0 ± 924.9 | 173.7 ± 12.4 | 138.7 ± 12.4 | 35.0 ± 0.8 | 2052.3 ± 912.4 | 734.9 ± 912.4 | 1317.4 ± 1290.4 | 0.67 | 0.08 |
| Scrivia | 44.71943° | 8.8602° | 8 | 18 03 2018 | 710.2 ± 125.9 | 298.9 ± 15.7 | 288.7 ± 15.7 | 10.2 ± 0.2 | 411.3 ± 110.1 | 232.6 ± 110.1 | 178.6 ± 155.8 | 0.58 | 0.57 |
| Senio | 44.2266° | 11.6324° | 19 | 15 07 2018 | 1269.4 ± 265.0 | 160.8 ± 17.9 | 126.1 ± 17.9 | 34.7 ± 0.8 | 1108.6 ± 247.1 | 280.5 ± 247.1 | 828.1 ± 349.4 | 0.53 | 0.14 |
| Serchio Filicaia | 44.1374° | 10.3741° | 4 | 15 07 2018 | 511.5 ± 68.9 | 109.1 ± 7.2 | 100.2 ± 7.2 | 8.9 ± 0.2 | 402.4 ± 61.7 | ND | ND | 0.57 | 0.28 |
| Taro | 44.6976° | 10.0934° | 12 | 21 03 2018 | 1598.0 ± 326.0 | 422.2 ± 22.7 | 407.8 ± 22.7 | 14.4 ± 0.3 | 1175.8 ± 303.3 | 745.5 ± 303.3 | 430.3 ± 428.9 | 0.84 | 0.29 |
| Taro | 44.6975° | 10.0936° | 12 | 15 07 2018 | 1598.0 ± 326.0 | 350.1 ± 24.3 | 325.3 ± 24.3 | 24.8 ± 0.6 | 1247.9 ± 301.6 | 791.2 ± 301.6 | 456.7 ± 426.6 | 0.84 | 0.23 |
| Trebbia | 44.9081° | 9.5897° | 10 | 22 03 2018 | 1171.3 ± 593.6 | 323.8 ± 18.4 | 310.2 ± 18.4 | 13.6 ± 0.3 | 847.5 ± 575.2 | 508.8 ± 575.2 | 338.7 ± 813.4 | 0.82 | 0.31 |
| Trebbia | 44.90890° | 9.5893° | 10 | 15 07 2018 | 1171.3 ± 593.6 | 79.1 ± 10.3 | 41.2 ± 10.3 | 37.9 ± 0.9 | 199.1 ± 32.1 | 119.6 ± 32.1 | 79.6 ± 45.4 | 0.82 | 1.30 |
| Vara | 44.1897° | 9.8578° | 6 | 20 03 2018 | 278.3 ± 42.4 | 62.6 ± 6.0 | 42.5 ± 6.0 | 20.1 ± 0.5 | 215.7 ± 36.4 | 39.8 ± 36.4 | 175.9 ± 51.4 | 1.47 | 0.27 |
| Vara | 44.1919° | 9.8584° | 6 | 15 07 2018 | 278.3 ± 42.4 | 104.8 ± 13.6 | 75.4 ± 13.6 | 29.4 ± 0.7 | 173.5 ± 28.8 | 32.0 ± 28.8 | 141.5 ± 40.7 | 1.47 | 0.58 |

D = Denudation flux (physical erosion + chemical weathering); $W_{Total}$ = Total Weathering Flux; $W_{Carb}$* = Adjusted Carbonate Weathering Flux; $W_{Sil}$ = Silicate Weathering Flux; $E_{Total}$* = Total Physical Erosion flux; $E_{Carb}$* = Carbonate Physical Erosion Flux; $E_{Sil}$* = Silicate Physical Erosion Flux.

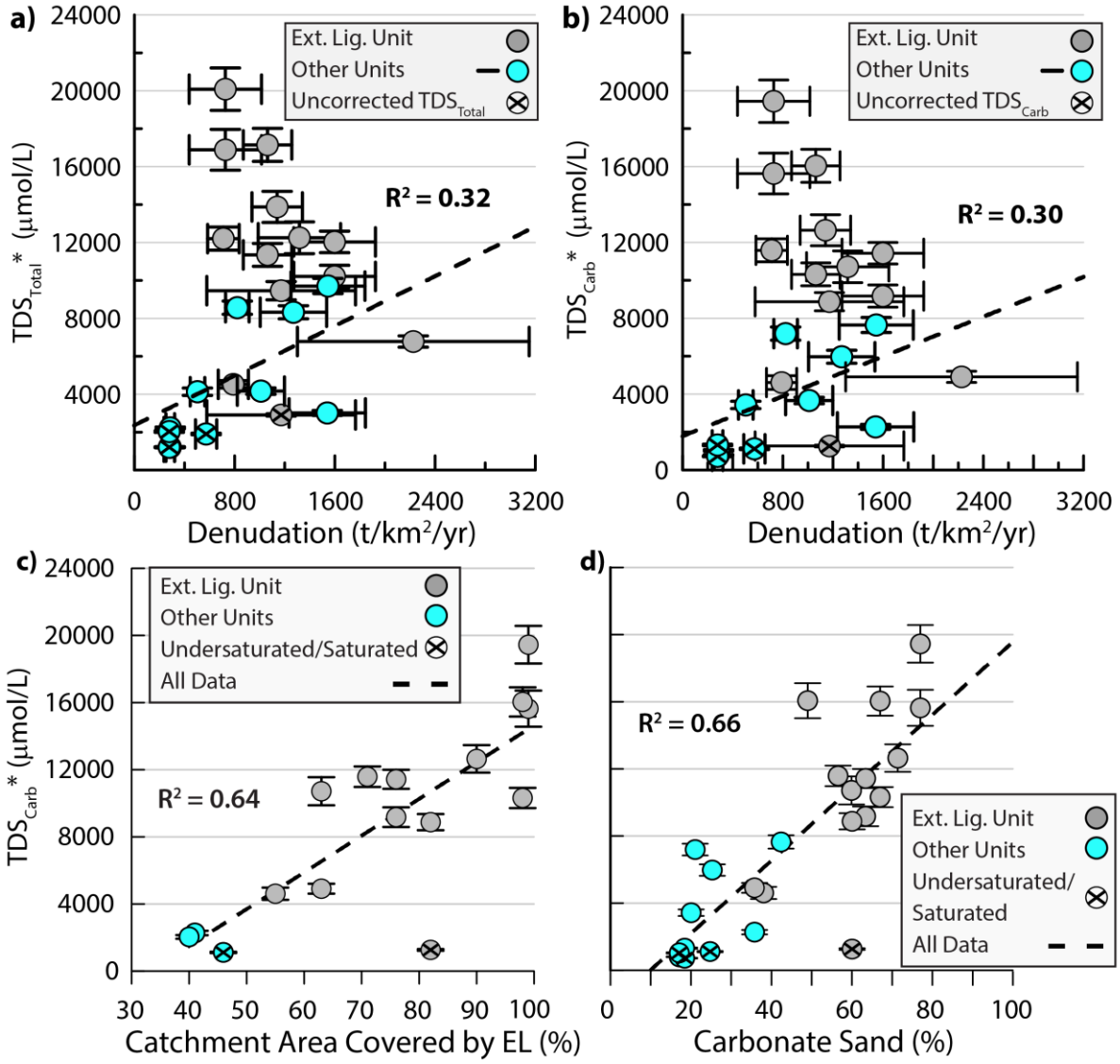


**Figure 10**. a) and b) Denudation fluxes plotted against a) $TDS_{Total}$* and b) $TDS_{Carb}$*. Linear regression applies only to oversaturated non-EL samples. c) and d) $TDS_{Carb}$* plotted against c) percent catchment area covered by the EL and d) percent carbonate sand. Dashed line reflects linear regression and $R^2$ statistic for the entire dataset. For all panels, samples draining the EL (gray circles) are distinguished from samples draining other lithologic units (cyan circles). No correction to $TDS_{Total}$ or $TDS_{Carb}$ was made for samples overlaid with an "x".

The strongest trends amongst these data are the increase in $TDS_{Carb}$* with 1) increasing catchment area covered by the EL and 2) with increasing percent carbonate sand. The former trend suggests a strong lithologic control on carbonate weathering rates in the Northern Apennines, where the EL provides higher $TDS_{Carb}$* concentrations and percent carbonate sand relative to the non-EL lithologies. The correlation between percent carbonate grains and

573 $TDS_{Carb}$* could reflect an increase of precipitated secondary carbonate sand grains with
574 increasing carbonate weathering fluxes. Alternatively, it could reflect erosion of primary
575 carbonates that correlates with weathering. Due to the lack of systematic constraints on the
576 fraction of primary versus secondary grains in the carbonate sand, we are unable to exclude
577 either one of these interpretations. We note, however, that while the fraction of secondary
578 carbonate grains (up to 35%) measured in catchments draining the Marnoso Arenacea Unit
579 (Cavazza, 1993) is substantial, it cannot solely explain the observed increase in carbonate sand
580 grains from 20% to 80% carbonate sand across the entire dataset (Figure 10d).
581
582 These patterns can also be interpreted in the context of the subsurface weathering zone (SWZ),
583 distinct from observations of the exported weathering fluxes derived from river waters. Here, we
584 infer that the EL catchments could reflect a "supply" limit, in that $TDS_{Carb}$* increases with a
585 greater supply of the EL (and presumably therefore higher average bedrock carbonate
586 concentrations across the catchment). We note, however, that the theoretical definition of the
587 supply limit predicts a strong correlation of weathering and denudation and a complete
588 dissolution of all minerals supplied to the weathering zone (West et al., 2005; Gabet and Mudd,
589 2009). Such a limit is unlikely in the EL, as we observe an abundance of primary carbonate in
590 river sands in EL catchments (e.g. Baganza River, Figure S6) and the absence of a correlation
591 between denudation fluxes and $TDS_{Total}$* or $TDS_{Carb}$* (Figure 10a-b). These observations suggest
592 instead that acid availability may ultimately limit weathering in the SWZ. Similarly, weathering
593 for EL catchments also appears to be limited in the river water (i.e. exported weathering fluxes),
594 based on the supersaturation of river waters and the decoupling observed between denudation
595 and metrics of weathering (Figure 5), albeit at a different acid limit than present in the SWZ.
596
597 The interpretation of the controls on weathering limits within the non-EL units is more
598 complicated. The evidence for a supply limit within the SWZ is tenuous, due to the weak
599 correlation between denudation and $TDS_{Total}$* ($R^2$=0.32) or $TDS_{Carb}$* ($R^2$=0.30) (Figure 10) for
600 oversaturated samples. In contrast with the EL Units, however, we observe a moderate, negative
601 correlation between $TDS_{Carb}$* and runoff ($R^2$=-0.58) (Figure 11a) and between $TDS_{Carb}$* and
602 $[SO_4^{2}]$ ($R^2$=0.44). The increase of $TDS_{Carb}$* with decreasing runoff (Figure 11a) suggests that
603 dilution may affect the magnitude of carbonate weathering from non-EL Units. Given the

additional negative correlation in the Northern Apennines between runoff and denudation, decreasing dilution with increasing denudation may explain the apparent (albeit weak) correlation between $TDS_{Carb}$* and denudation (Figure 10a-b). For example, we note that all undersaturated samples were collected during the winter/spring season, when runoff is highest, suggesting that dilution may play a role in the concentrations we measure, although we require more systematic sampling of the winter and summer seasons to properly address this point.

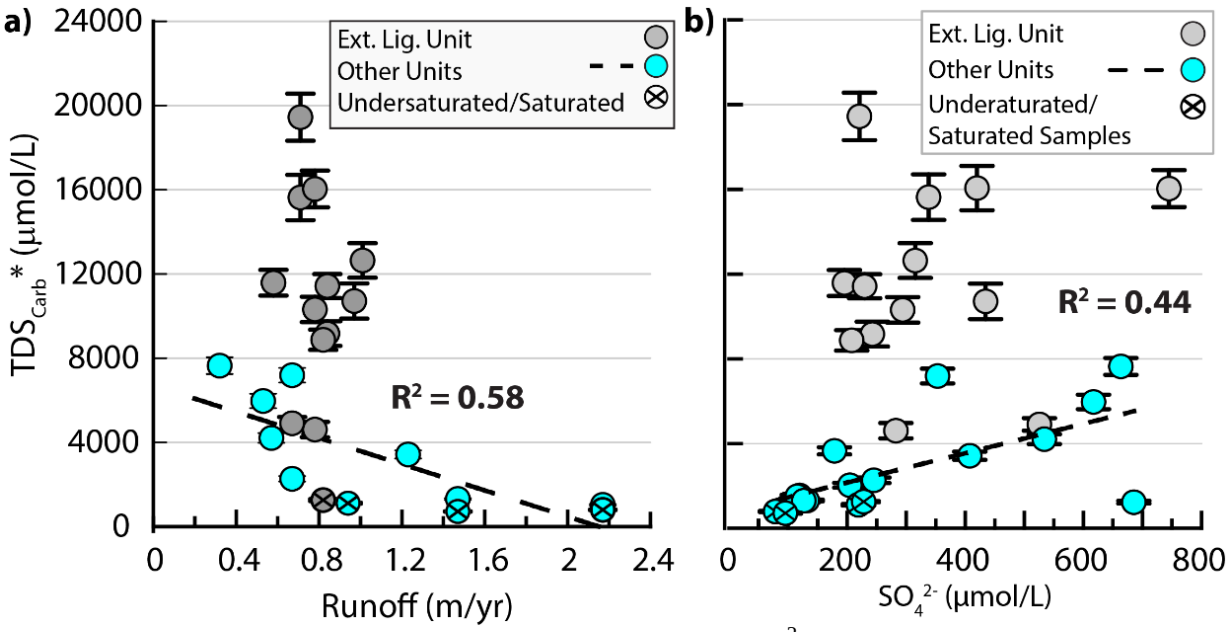


**Figure 11**. a) Runoff plotted against $TDS_{Carb}$* and b) [$SO_4^{2-}$] plotted against $TDS_{Carb}$*. Linear regressions refer to samples from Other Units (all cyan circles).

We recognize that denudation fluxes from [$^{10}$Be] record weathering down to depths of only 60 cm (Riebe and Granger, 2013), while the SWZ may in fact be many meters deep (Uhlig et al., 2020). If weathering occurs at depths of greater than a few meters, it is capable of contributing to the overall denudation flux without affecting [$^{10}$Be]. In turn, this may result in an overall underestimation of the measured denudation flux (Riebe and Granger, 2013). Our data support the idea that a substantial portion of the SWZ fluxes likely occurs below 60 cm depth, and thus may not be reflected in the total $^{10}$Be denudation flux. However, we may further be underestimating the physical erosion flux because [$^{10}$Be] will only reflect the denudation of primary sand grains formed in the SWZ, whereas the carbonate sand fraction we measured reflects both primary and secondary grains. If a substantial portion of the weathering occurs beneath 60 cm, and then a large portion of this dissolved carbonate is re-precipitated, the total

626 erosion flux at the orogen front will be greater than that estimated by [$^{10}$Be]. To estimate this
627 effect, we quantify the flux of initially weathered carbonate that has been converted back to solid
628 grains (ie, the secondary carbonate erosion flux) for each catchment, by assuming that the
629 difference between [$Ca^{2+}$*] and [$Ca^{2+}$] represents re-precipitation of calcium carbonate (Table
630 S4). These fluxes vary from 0–1,234 t/km$^2$/yr. Astonishingly, for 3 EL catchments, this
631 secondary carbonate erosion flux is higher than the total denudation flux. For all other
632 catchments, the secondary carbonate erosion flux varies from 0–82% of the total denudation
633 flux, with median and average values of 35% and 44%, respectively (Table S4). Though these
634 exact numbers require certainty about the bedrock Sr/Ca and the partition coefficient between
635 dissolved [$Sr^{2+}$] and carbonate Sr/Ca, they illustrate the importance of secondary carbonate
636 precipitation in mixed lithology landscapes.
637
638 Thus far, we have assumed that carbonic acid is the primary weathering agent in the Northern
639 Apennines. Sulfuric acid sourced from the oxidation of sulfide minerals is an important
640 additional source of acidity in a number of mountain ranges (Calmels et al., 2007; Emberson et
641 al., 2016; Blattmann et al., 2019) and a source of dissolved sulfate, $SO_4^{2-}$. The production of
642 sulfuric acid has been observed in a number of caves in northern and central Italy, and has been
643 associated with sulfate reduction of Triassic gypsum/anhydrite deposits (Angeli et al., 2019).
644 This sulfuric acid could surface either through connections between karst springs and river
645 channels (Chiesi et al., 2010) or by faulting (Angeli et al., 2019). Further, minor pyrite in
646 sedimentary units could be a source of sulfuric acid (Cortecci et al., 2008). Quantifying the
647 contribution of sulfuric acid to weathering in the northern Apennines would require constraining
648 evaporite contributions to sulfate using sulfur isotopes. Nevertheless, we propose that sulfuric
649 acid cannot be the dominant control on carbonate weathering in the northern Apennines, given
650 that [$SO_4^{2-}$] are, for the most part, more than an order of magnitude lower than $TDS_{carb}$* (Figure
651 11b). In addition, [$SO_4^{2-}$] are uncorrelated with $TDS_{carb}$* in catchments draining the EL units. In
652 contrast, we observe a moderate correlation between dissolved sulfate and $TDS_{carb}$*, which
653 suggests a potential contribution of sulfuric acid to carbonate weathering in these catchments.
654
655 **5.3.4 Carbonate Weathering and Precipitation Pathways in the Northern Apennines**

Here, we summarize the preceding discussion in the context of (1) where carbonate weathering and secondary re-precipitation occur in the landscape, and (2) the limits on carbonate weathering across the landscape (Figure 12). The subsurface is comprised of mixed carbonate-siliciclastic bedrock and the overlying sediment and soil that compose the SWZ. For simplicity, however, we illustrate only the pathways for carbonate sediments in this landscape. Solute compositions in soil waters correspond to the concentrations adjusted for secondary re-precipitation—the weathering zone conditions. In the SWZ, plant respiration (white arrows) produces soil $CO_2$, which interacts with soil water to form carbonic acid (Romero-Mujalli et al., 2018). High $pCO_2$ in the soil water (represented by full conical flask symbols) allows a relatively large volume of carbonate to be dissolved in the subsurface, although, based on the presence of primary calcite grains, it is still insufficient to dissolve the abundant supply of carbonate in Northern Apennine rivers (Figure 10b-d).

The dissolution of carbonate rock produces $HCO_3^-$ and $Ca^{2+}$ ions, which are discharged to rivers (blue arrows). Here, $CO_2$-charged soil water equilibrates with atmospheric $pCO_2$ by degassing excess $CO_2$ (black gradient arrows). This loss of acidity and subsequent pH increase leads to supersaturation of the water with respect to carbonate. Secondary carbonate is thus re-precipitated in the river channel (dashed gray arrows in river channel), particularly along steep sections of the river channel with highly turbulent flow (e.g. waterfalls or catch dams). As a result, the river sediments in the channel are a mix of primary carbonate grains (gray sediment in river channel) and secondary carbonate grains (white sediment in river channel). Given the large initial weathering fluxes and secondary carbonate erosion fluxes that we calculate, it may even be that much of the secondary carbonate precipitation occurs within the SWZ—before entering the river channel—such that there are large dissolution and re-precipitation fluxes within the SWZ. Such fluxes would concentrate Sr/Ca in soil waters and imply that the SWZ has far more dynamic dissolution and re-precipitation fluxes than previously suspected for carbonate-rich landscapes.

The initial dissolution and subsequent secondary precipitation of carbonate grains results in a decoupling between the limits on the dissolved carbonate flux in soil waters and in river waters. In the SWZ, carbonate weathering is most likely limited by the $pCO_2$ of soils. Between the EL

687 versus non-EL units, differences in acid availability may reflect differences in primary porosity,
688 agricultural practices, or vegetation. We also cannot exclude dilution as a control on carbonate
689 weathering in the non-EL Units, although the pattern of rainfall and snowfall in the Northern
690 Apennines suggests that it may be more important during the winter months. The magnitude and
691 importance of weathering within the SWZ is further illustrated by the ratio of erosion to
692 weathering fluxes (E/W = 4), as reflected in the weathering zones fluxes.
693
694 Once solutes are discharged to streams, the total export of [$Ca^{2+}$] becomes limited by acid
695 availability in the stream due to equilibration with atmospheric $pCO_2$. Thus, the export of [$Ca^{2+}$]
696 becomes decoupled from the processes in the weathering zone and will instead be limited by the
697 rates of in-stream $CO_2$ degassing and secondary precipitation of calcite, with the ultimate limit
698 being set by the $pCO_2$ in the atmosphere and the quantity of organic matter re-mineralized in
699 river water. The grains and travertine deposits that are newly formed by secondary calcite once
700 again join the physical denudation flux and the export of sediment from mountains. Additional
701 dissolution may occur downstream in floodplains when undersaturated floodplain waters interact
702 with oversaturated mountain streams. Samples collected from mountain streams will reflect the
703 erosion to weathering ratios (E/W = 24) of our exported fluxes. We surmise that upstream
704 reaches of the river could have lower ratios in between those calculated for the SWZ and for
705 exported river fluxes, whereas, at the orogen front, E/W ratios will be even higher, given the
706 importance of secondary carbonate physical erosion in this landscape. Thus, the processes of
707 secondary precipitation and dissolution provide a bridge between physical and chemical erosion
708 of carbonate rock that has to be considered in order to quantify the coupling between mountain
709 uplift and denudation.
710

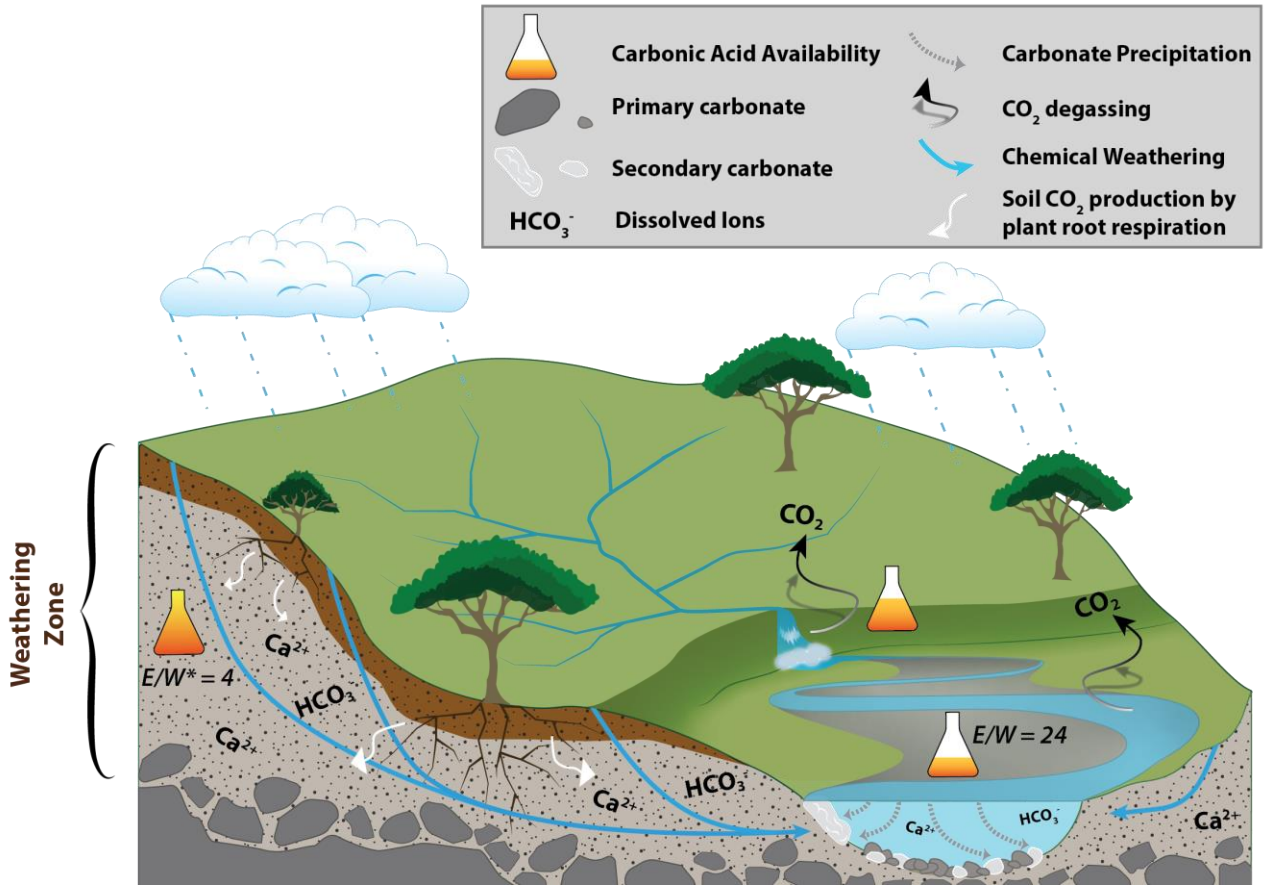


**Figure 12.** Schematic of weathering pathways in the Northern Apennines, illustrating the locations of carbonate weathering and re-precipitation processes in the subsurface and at the surface, respectively. E/W numbers refer to calculated ratios of erosion to weathering at different points on the landscape, dependent upon the degree to which carbonate has been re-precipitated between initial dissolution and export from the mountain front.

## 6 Conclusions

In this study, we partition denudation fluxes into physical erosion and chemical weathering fluxes for both carbonates and silicates, in an orogenic setting with mixed siliciclastic-carbonate lithologies. Physical erosion dominates the denudation fluxes, and the proportion of carbonate and silicate in the physical erosion flux is apparently controlled, to first order, by the composition of the bedrock. In contrast, carbonate weathering fluxes dominate the total weathering signal irrespective of the lithology, although the exposure of the External Ligurian Unit in catchments appears to systematically raise carbonate weathering in the weathering zone.

727 Relative to other orogens, the ratio of erosion to total weathering (E/W) is smaller in the
728 Northern Apennines, due to generally higher total weathering fluxes. In the Northern Apennines,
729 carbonate weathering represents an important component of the total weathering flux, and
730 secondary calcite precipitation is ubiquitous. This process converts dissolved riverine solutes
731 back into solid carbonate and, we estimate that 20–90% of [$Ca^{2+}$] is lost to precipitation of
732 secondary calcite.
733
734 We conclude that the controls on carbonate weathering vary across the landscape. In the
735 weathering zone, carbonate weathering appears to be limited by the partial pressure of $CO_2$ in
736 soils, but the discharge of waters to rivers and the equilibration with atmospheric $pCO_2$
737 fundamentally alter this limit. In rivers, the concentration of dissolved carbonates becomes
738 limited instead by the rates of $CO_2$ degassing and secondary carbonate precipitation. As a
739 consequence, the exported volume of solutes from mountain catchments becomes, at least in
740 part, decoupled from subsurface weathering-zone processes.
741
742 The results from this study advance our understanding of denudational processes in a young
743 mountain range that typifies the initial stages of orogenesis. We have shown that understanding
744 the weathering and erosional processes of carbonate in a thermodynamically limited landscape
745 requires quantifying both the primary processes responsible for carbonate erosion and
746 weathering, as well as the secondary processes responsible for the re-precipitation of carbonates
747 and re-introduction of physical carbonate into the river channels.
748

## Acknowledgments, Samples, and Data

The authors declare no conflicts of interest with respect to the results of this paper. Supporting material to this manuscript can be found in the supplementary material. The $^{10}$Be catchment-averaged denudation rate data (Erlanger, 2020) that support the findings of this study are openly available in the ETH Zürich Research Collection "Erosion and weathering of the Northern Apennines with implications for the tectonic and kinematics of the orogen" at https://doi.org/10.3929/ethz-b-000393261.

Funding was provided by the Swiss National Science Foundation (SNSF) SINERGIA Swiss Alp Array project (SNF #154434). JKCR was supported by an ETH Fellowship and an Alexander von Humboldt Postdoctoral Fellowship.

## References

Angeli, I.M.D., Parise, M., Vattano, M., Madonia, G., Galdenzi, S., and Waele, J. De, 2019, Geomorphology Sulfuric acid caves of Italy : A review: v. 333, p. 105–122, doi:10.1016/j.geomorph.2019.02.025.

Bickle, M.J., Chapman, H.J., Bunbury, J., Harris, N.B.W., Fairchild, I.J., Ahmad, T., and Pomiès, C., 2005, Relative contributions of silicate and carbonate rocks to riverine Sr fluxes in the headwaters of the Ganges: Geochimica et Cosmochimica Acta, v. 69, p. 2221–2240, doi:10.1016/j.gca.2004.11.019.

Bickle, M.J., Tipper, E., Galy, A., Chapman, H., and Harris, N., 2015, On discrimination between carbonate and silicate inputs to Himalayan rivers: American Journal of Science, v. 315, p. 120–166, doi:10.2475/02.2015.02.

Blattmann, T.M., Wang, S.-L., Lupker, M., Maerki, L., Haghipour, N., Wacker, L., Chung, L.-H., Bernasconi, S.M., Ploetze, M., and Eglinton, T.., 2019, Sulphuric acid-mediated weathering on Taiwans buffers geological atmospheric carbon sinks: Nature Scientific Reports, p. 3–10, doi:10.1038/s41598-019-39272-5.

Brandon, M.T., and Vance, J.A., 1992, Tectonic evolution of the Cenozoic Olympic subduction complex, Washington State, as deduced from fission track ages for detrial zircons: American Journal of Science, v. 292, p. 565.

Brunetti, M., Maugeri, M., Nanni, T., Simolo, C., and Spinoni, J., 2014, High-resolution temperature climatology for Italy: Interpolation method intercomparison: International Journal of Climatology, v. 34, p. 1278–1296, doi:10.1002/joc.3764.

Calmels, D., Gaillardet, J., Brenot, A., and France-Lanord, C., 2007, Sustained sulfide oxidation by physical erosion processes in the Mackenzie River basin: Climatic perspectives:

Geology, v. 35, p. 1003–1006, doi:10.1130/G24132A.1.

Calmels, D., Galy, A., Hovius, N., Bickle, M., West, A.J., Chen, M.C., and Chapman, H., 2011, Contribution of deep groundwater to the weathering budget in a rapidly eroding mountain belt, Taiwan: Earth and Planetary Science Letters, v. 303, p. 48–58, doi:10.1016/j.epsl.2010.12.032.

Cantonati, M., Segadelli, S., Ogata, K., Tran, H., Sanders, D., Gerecke, R., Rott, E., Filippini, M., Gargini, A., and Celico, F., 2016, A global review on ambient Limestone-Precipitating Springs (LPS): Hydrogeological setting, ecology, and conservation: Science of the Total Environment, v. 568, p. 624–637, doi:10.1016/j.scitotenv.2016.02.105.

Carlini, M., Chelli, A., Vescovi, P., Artoni, A., Clemenzi, L., Tellini, C., and Torelli, L., 2016, Tectonic control on the development and distribution of large landslides in the Northern Apennines (Italy): Geomorphology, v. 253, p. 425–437, doi:10.1016/j.geomorph.2015.10.028.

Carretier, S., Regard, V., Vassallo, R., Martinod, J., Christophoul, F., Gayer, E., Audin, L., and Lagane, C., 2015, A note on 10Be-derived mean erosion rates in catchments with heterogeneous lithology: Examples from the western Central Andes: Earth Surface Processes and Landforms, v. 40, p. 1719–1729, doi:10.1002/esp.3748.

Cavazza, W., 1993, Sedimentary recycling in a temperate climate drainage basin (Senio River, north-central Italy): composition of source rock, soil profiles, and fluvial deposits: Geological Society of America Special Paper, v. 284, p. 247–261.

Caves Rugenstein, J.K., Ibarra, D.E., and von Blanckenburg, F., 2019, Neogene cooling driven by land surface reactivity rather than increased weathering fluxes: Nature, v. 571, p. 99–102, doi:10.1038/s41586-019-1332-y.

Chiesi, M., Waele, J. De, and Forti, P., 2010, Origin and evolution of a salty gypsum / anhydrite karst spring : the case of Poiano ( Northern Apennines , Italy ): , p. 1111–1124, doi:10.1007/s10040-010-0576-2.

Cortecci, G., Dinelli, E., Bencini, A., Adorni-Braccesi, A., and La Ruffa, G., 2002, Natural and anthropogenic SO4 sources in the Arno river catchment, northern Tuscany, Italy: A chemical and isotopic reconnaissance: Applied Geochemistry, v. 17, p. 79–92, doi:10.1016/S0883-2927(01)00100-7.

Cortecci, G., Dinelli, E., Boschetti, T., and Arbizzani, P., 2008, The Serchio River catchment ,

northern Tuscany: Geochemistry of stream waters and sediments, and isotopic composition of dissolved sulfate: Applied Geochemistry, v. 23, p. 1513–1543, doi:10.1016/j.apgeochem.2007.12.031.

Crespi, A., Brunetti, M., Lentini, G., and Maugeri, M., 2018, 1961–1990 high-resolution monthly precipitation climatologies for Italy: International Journal of Climatology, v. 38, p. 878–895, doi:10.1002/joc.5217.

Cyr, A.J., and Granger, D.E., 2008, Dynamic equilibrium among erosion, river incision, and coastal uplift in the northern and central Apennines, Italy: Geology, v. 36, p. 103–106, doi:10.1130/G24003A.1.

Cyr, A.J., Granger, D.E., Olivetti, V., and Molin, P., 2014, Distinguishing between tectonic and lithologic controls on bedrock channel longitudinal profiles using cosmogenic10Be erosion rates and channel steepness index: Geomorphology, v. 209, p. 27–38, doi:10.1016/j.geomorph.2013.12.010.

Davies, C.W., and Shedlovsky, T., 1964, Ion association: Journal of The Electrochemical Society, v. 111, p. 85C-86C.

Dercourt, J., and Vrielynck, B., 1993, Atlas Tethys paleoenvironmental maps: Gauthier-Villars.

Drake, J.J., and Wigley, T.M.L., 1975, The effect of climate on the chemistry of carbonate groundwater: Water resources research, v. 11, p. 958–962.

Emberson, R., Galy, A., and Hovius, N., 2017, Combined effect of carbonate and biotite dissolution in landslides biases silicate weathering proxies: Geochimica et Cosmochimica Acta, v. 213, p. 418–434, doi:10.1016/j.gca.2017.07.014.

Emberson, R., Galy, A., and Hovius, N., 2018, Weathering of Reactive Mineral Phases in Landslides Acts as a Source of Carbon Dioxide in Mountain Belts: Journal of Geophysical Research: Earth Surface, p. 2695–2713, doi:10.1029/2018JF004672.

Emberson, R., Hovius, N., Galy, A., and Marc, O., 2016, Oxidation of sulfides and rapid weathering in recent landslides: Earth Surface Dynamics, v. 4, p. 727–742, doi:10.5194/esurf-4-727-2016.

Erlanger, E.D., 2020, Erosion and weathering of the Northern Apennines with implications for the tectonics and kinematics of the orogen: ETH Zürich, 149 p.

Fellin, M.G., Reiners, P.W., Brandon, M.T., Wüthrich, E., Balestrieri, M.L., and Molli, G., 2007, Thermochronologic evidence for the exhumational history of the Alpi Apuane metamorphic

core complex, northern Apennines, Italy: Tectonics, v. 26, p. 1–22, doi:10.1029/2006TC002085.

Gabet, E.J., and Mudd, S.M., 2009, A theoretical model coupling chemical weathering rates with denudation rates: Geology, v. 37, p. 151–154, doi:10.1130/G25270A.1.

Gaillardet, J., Calmels, D., Romero-Mujalli, G., Zakharova, E., and Hartmann, J., 2018, Global climate control on carbonate weathering intensity: Chemical Geology, p. 1–11, doi:10.1016/j.chemgeo.2018.05.009.

Gaillardet, J., Dupré, B., Louvat, P., and Allègre, C.J., 1999, Global silicate weathering and CO2 consumption rates deduced from the chemistry of large rivers: Chemical Geology, v. 159, p. 3–30, doi:10.1016/S0009-2541(99)00031-5.

Garzanti, E., Canclini, S., Moretti Foggia, F., and Petrella, N., 2002, Unraveling magmatic and orogenic provenances in modern sands: the back-arc side of the Apennine thrust-belt (Italy): Journal of Sedimentary Research, v. 72, p. 2–17, doi:10.1306/051801720002.

Garzanti, E., Scutellà, M., and Vidimari, C., 1998, Provenance from ophiolites and oceanic allochtons: Modern beach and river sands from Liguria and the northern Apennines (Italy): Ofioliti, v. 23, p. 65–82.

Goddéris, Y., Donnadieu, Y., Carretier, S., Aretz, M., Dera, G., MacOuin, M., and Regard, V., 2017, Onset and ending of the late Palaeozoic ice age triggered by tectonically paced rock weathering: Nature Geoscience, v. 10, p. 382–386, doi:10.1038/ngeo2931.

Granger, D.E., Kirchner, J.W., and Finkel, R., 1996, Spatially Averaged Long-Term Erosion Rates Measured from in Situ-Produced Cosmogenic Nuclides in Alluvial Sediment: The Journal of Geology, v. 104, p. 249–257, doi:10.1086/629823.

Hilton, R.G., and West, A.J., 2020, Mountains, erosion and the carbon cycle: Nature Reviews Earth & Environment, v. 1, p. 284–299.

Jacobson, A.D., and Blum, J.D., 2003, Relationship between mechanical erosion and atmospheric CO2 consumption in the New Zealand Southern Alps: Geology, p. 865–868.

Jacobson, A.D., Blum, J.D., Chamberlain, C.P., Craw, D., and Koons, P.O., 2003, Climatic and tectonic controls on chemical weathering in the New Zealand Southern Alps: Geochimica et Cosmochimica Acta, v. 67, p. 29–46.

Kirchner, J.W., Finkel, R.C., Riebe, C.S., Granger, D.E., Clayton, J.L., King, J.G., Megahan, W.F., and Sites, F., 2001, Mountain erosion over 10 yr , 10 k.y., and 10 m.y. time scales:

Geology, v. 29, p. 591–594, doi:10.1130/0091-7613(2001)029<0591:MEOYKY>2.0.CO;2.

Langmuir, D., 1971, The geochemistry of some carbonate ground waters in central Pennsylvania: Geochimica et Cosmochimica Acta, v. 35, p. 1023–1045, doi:https://doi.org/10.1016/0016-7037(71)90019-6.

Larsen, I.J., Montgomery, D.R., and Greenberg, H.M., 2014, The contribution of mountains to global denudation: Geology, v. 42, p. 527–530, doi:10.1130/G35136.1.

Matmon, A., Bierman, P.R., Larsen, J., Southworth, S., Pavich, M., Finkel, R., and Caffee, M., 2003, Erosion of an ancient mountain range, the Great Smoky Mountains, North Carolina and Tennessee: American Journal of Science, v. 303, p. 817–855.

Milliman, J.D., and Farnsworth, K.L., 2011, River discharge to the coastal ocean: A global synthesis: River Discharge to the Coastal Ocean: A Global Synthesis, p. 1–384, doi:10.1017/CBO9780511781247.

Molli, G., 2008, Northern Apennine–Corsica orogenic system: an updated overview: Geological Society, London, Special Publications, v. 298, p. 413–442, doi:10.1144/SP298.19.

Moore, J., Jacobson, A.D., Holmden, C., and Craw, D., 2013, Tracking the relationship between mountain uplift, silicate weathering, and long-term CO2 consumption with Ca isotopes: Southern Alps, New Zealand: v. 341, p. 110–127, doi:10.1016/j.chemgeo.2013.01.005.

Ott, R.F., 2020, How lithology impacts global topography, vegetation, and animal biodiversity: A global-scale analysis of mountainous regions: Geophysical Research Letters, v. 47, p. e2020GL088649.

Ott, R.F., Gallen, S.F., Wegmann, K.W., Biswas, R.H., Herman, F., and Willett, S.D., 2019, Pleistocene terrace formation, Quaternary rock uplift rates and geodynamics of the Hellenic Subduction Zone revealed from dating of paleoshorelines on Crete, Greece: Earth and Planetary Science Letters, v. 525, p. 115757.

Philip, J., Masse, J.-P., and Camoin, G., 1996, Tethyan Carbonate Platforms BT - The Tethys Ocean, *in* Nairn, A.E.M., Ricou, L.-E., Vrielynck, B., and Dercourt, J. eds., Boston, MA, Springer US, p. 239–265, doi:10.1007/978-1-4899-1558-0_8.

Le Pichon, X., Pautot, G., Auzende, J.-M., and Olivet, J.-L., 1971, La Mediterranee occidentale depuis l'Oligocene Schema d'evolution: Earth and Planetary Science Letters, v. 13, p. 145–152, doi:https://doi.org/10.1016/0012-821X(71)90117-8.

Ricci Lucchi, F., 1986, The Oligocene to Recent foreland basins of the northern Appennines:

907 Foreland Basins, p. 105–140.
908 Riebe, C.S., and Granger, D.E., 2013, Quantifying effects of deep and near-surface chemical
909 erosion on cosmogenic nuclides in soils, saprolite, and sediment: Earth Surface Processes
910 and Landforms, v. 38, p. 523–533, doi:10.1002/esp.3339.
911 Riebe, C.S., Kirchner, J.W., Granger, D.E., and Finkel, R.C., 2001, Minimal climatic control on
912 erosion rates in the Sierra Nevada , California: , p. 447–450.
913 Romero-Mujalli, G., Hartmann, J., Börker, J., Gaillardet, J., and Calmels, D., 2018, Ecosystem
914 controlled soil-rock pCO2 and carbonate weathering - Constraints by temperature and soil
915 water content: Chemical Geology, doi:10.1016/j.chemgeo.2018.01.030.
916 Sarin, M.M., Krishnaswami, S., Dilli, K., Somayajulu, B.L.K., and Moore, W.S., 1989, Major
917 ion chemistry of the Ganga-Brahmaputra river system: Weathering processes and fluxes to
918 the Bay of Bengal: Geochimica et Cosmochimica Acta, v. 53, p. 997–1009,
919 doi:10.1016/0016-7037(89)90205-6.
920 Segadelli, S., and de Nardo, M.T., 2018, Sorgenti e travertini nell'Appennino emiliano-
921 romagnolo: studio a scala regionale per un quadro conoscitivo complessivo e cartografico
922 delle sorgenti "pietrificanti" (LPS):
923 Segadelli, S., Vescovi, P., Ogata, K., Chelli, A., Zanini, A., Boschetti, T., Petrella, E., Toscani,
924 L., Gargini, A., and Celico, F., 2017, A conceptual hydrogeological model of ophiolitic
925 aquifers (serpentinised peridotite): The test example of Mt. Prinzera (Northern Italy):
926 Hydrological Processes, v. 31, p. 1058–1073.
927 Stallard, R.F., and Edmond, J.M., 1981, Geochemistry of the Amazon: 1. Precipitation chemistry
928 and the marine contribution to the dissolved load at the time of peak discharge: Journal of
929 Geophysical Research: Oceans, v. 86, p. 9844–9858, doi:10.1029/JC086iC10p09844.
930 Stallard, R.F., and Edmond, J.M., 1987, Geochemistry of the Amazon: 3. Weathering chemistry
931 and limits to dissolved inputs: Journal of Geophysical Research: Oceans, v. 92, p. 8293–
932 8302.
933 Summerfield, M.A., and Hulton, N.J., 1994, Natural controls of fluvial denudation rates in major
934 world drainage basins: Journal of Geophysical Research: Solid Earth, v. 99, p. 13871–
935 13883, doi:10.1029/94jb00715.
936 Torres, M.A., West, A.J., Clark, K.E., Paris, G., Bouchez, J., Ponton, C., Feakins, S.J., Galy, V.,
937 and Adkins, J.F., 2016, The acid and alkalinity budgets of weathering in the Andes–

Amazon system: Insights into the erosional control of global biogeochemical cycles: Earth and Planetary Science Letters, v. 450, p. 381–391, doi:10.1016/j.epsl.2016.06.012.

Uhlig, D., Amelung, W., and von Blanckenburg, F., 2020, Mineral Nutrients Sourced in Deep Regolith Sustain Long-Term Nutrition of Mountainous Temperate Forest Ecosystems: Global Biogeochemical Cycles, v. 34, doi:10.1029/2019GB006513.

Vai, F., and Martini, I.P., 2001, Anatomy of an orogen: the Apennines and adjacent Mediterranean basins: Springer.

West, A.J., Galy, A., and Bickle, M., 2005, Tectonic and climatic controls on silicate weathering: Earth and Planetary Science Letters, v. 235, p. 211–228, doi:10.1016/j.epsl.2005.03.020.

Wittmann, H., Malusà, M.G., Resentini, A., Garzanti, E., and Niedermann, S., 2016, The cosmogenic record of mountain erosion transmitted across a foreland basin: Source-to-sink analysis of in situ 10Be, 26Al and 21Ne in sediment of the Po river catchment: Earth and Planetary Science Letters, v. 452, p. 258–271, doi:10.1016/j.epsl.2016.07.017.